Structure of the complete, membrane-assembled COPII coat reveals a complex interaction network.

Joshua Hutchings[1], Viktoriya G. Stancheva[2], Nick R. Brown[1,3], Alan M.C. Cheung[1,4], Elizabeth A. Miller[2] and Giulia Zanetti*[1].

[1]Institute of Structural and Molecular Biology, Birkbeck College, London

[2]MRC Laboratory of Molecular Biology, Cambridge

[3]Present address: The Francis Crick Institute, London

[4]Present address: School of Biochemistry at the University of Bristol

*correspondence: g.zanetti@bbk.ac.uk

Summary

The COPII coat mediates Endoplasmic Reticulum (ER) to Golgi trafficking of thousands of proteins. Five essential coat components assemble on the ER membrane to induce the formation of transport vesicles while selectively recruiting cargo proteins. Individual COPII proteins interact dynamically through multiple interfaces to assemble into inner and outer coat layers, forming coats of varied architectures.

Here we have used cryo-electron tomography (cryo-ET) and subtomogram averaging to visualise the complete membrane-bound COPII coat to unprecedented detail, revealing a complex interaction network that includes a number of previously unknown interfaces. We identify essential interactions, and functionally characterise their contribution to COPII assembly and membrane remodelling. We find that multiple finely-tuned interfaces contribute to coat organization required to remodel membranes, depending additionally on membrane properties. Our work sheds light on how COPII transports the diverse range of cargo molecules required by the cell.

Introduction

Eukaryotic cells are organized in membrane-bound compartments, and a tightly regulated trafficking system ensures proteins and lipids are delivered to the right place at the right time. Cytosolic coat proteins capture secretory cargo and sculpt membrane carriers for intracellular transport (Bonifacino and Glick, 2004). A third of all proteins in eukaryotic cells are synthesized in the Endoplasmic Reticulum (ER) and trafficked to the Golgi, destined for secretion or residency within organelles. ER export is mediated by the coat protein complex II (COPII), which minimally comprises five cytosolic proteins that form two concentric layers on the ER membrane – the inner and outer coat (Zanetti et al., 2012). The inner coat layer consists of the small GTPase Sar1 and the heterodimeric Sec23/24 complex, whilst the outer coat layer comprises the rod-shaped heterotetramer Sec13/31. COPII dynamically assembles and disassembles at ER exit sites, imparting enough force to bend the membrane into unfavourable conformations while at the same time maintaining a range of membrane curvatures. It remains unclear how the COPII coat achieves the required balance of strength and flexibility, and how this balance is regulated to form vesicles of different sizes and shapes, essential to transport a diverse range of cargo molecules (Hutchings and Zanetti, 2019).

COPII assembly begins with the formation of the inner coat, after GTP-bound Sar1 exposes an amphipathic helix for burial into the ER membrane (Hutchings et al., 2018; Lee et al., 2005). Sar1-GTP then recruits Sec23/24. Sec23 binds Sar1 and is the dedicated GTPase-activating protein (GAP) (Antonny et al., 2001; Barlowe et al., 1994; Bi et al., 2002), whilst Sec24 possesses multiple binding sites for cargo recruitment (Miller et al., 2003; Mossessova et al., 2003). Sec23 also recruits the outer coat subunits Sec13/31 through a flexible proline-rich domain (PRD) in the C-terminal half of Sec31, which accelerates the GAP activity of Sec23 (Bi et al., 2007). Both the inner and the outer coat are thought to oligomerise and induce membrane curvature to form coated membrane carriers (Hutchings et al., 2018; Stagg et al., 2006, 2008; Zanetti et al., 2013). COPII has been shown to generate vesicles and

tubules both *in vivo* and *in vitro*, suggesting the coat is adaptable for different morphologies (Bacia et al., 2011; Barlowe et al., 1994; Fromme et al., 2007; Gorur et al., 2017; Matsuoka et al., 1998a; Venditti et al., 2012; Zanetti et al., 2013). This is consistent with a need to maintain constitutive secretion of soluble proteins, whilst also accommodating much larger cargo such as procollagens and prechylomicrons in specialised mammalian cells (Gorur et al., 2017; Hutchings and Zanetti, 2019; Jin et al., 2012; Malhotra and Erlmann, 2015; Townley et al., 2008).

COPII assembly is governed by numerous interactions within and between the coat layers (Bi et al., 2007; Hutchings et al., 2018; Ma and Goldberg, 2016; Stagg et al., 2008). Lateral interactions between inner coat subunits mediate its polymerisation into arrays, which have been proposed to prime coat assembly and directly orient membrane curvature through Sar1 amphipathic helix insertion (Hutchings et al., 2018). Sec13/31 self-assembles into cages of different geometries *in vitro*, with a range of diameters consistent with isolated vesicles (Stagg et al., 2006, 2008). The edge elements of the cage comprise two structured domains in the N-terminal half of Sec31 – an N-terminal β-propeller that mediates tetrameric vertex contacts within the cage, and an α-solenoid domain that mediates homodimerisation of Sec31 (Fath et al., 2007). These domains are separated by a blade insertion motif, which binds the Sec13 β-propeller and rigidifies the rod-shaped assembly (Čopič et al., 2012; Fath et al., 2007). Downstream of these structured domains, the C-terminal half of Sec31 comprises a flexible proline-rich domain (PRD) and a putative helical C-terminal domain (CTD) (Fath et al., 2007). No role for the CTD has yet been assigned, but limited proteolysis experiments and secondary structure prediction suggest an ordered helical domain of ~18 kDa (Dokudovskaya et al., 2006; Paraan et al., 2018). The PRD mediates several interactions with Sec23 in the inner coat, including: i) a GAP-accelerating region that binds the Sar1-Sec23 interface (Bi et al., 2007), ii) triple-proline (PPP) motifs binding the tip of the Sec23 gelsolin domain that assist in the assembly of inner coat subunits (Hutchings et al., 2018; Ma and Goldberg, 2016), and iii) a recently defined charge-based interaction (Stancheva et al., 2020).

Some of the interaction interfaces, including outer-inner coat interactions mediated by PPP motifs and the Sec31 active peptide, as well as cage vertices, have been characterized structurally. Disruption of many of these interfaces are tolerated individually but not in combination, implying a network of partially redundant interactions that collectively stabilise coat assembly (Hutchings et al., 2018; Stancheva et al., 2020). For instance, partial disruption of outer coat polymerisation by means of an N-terminal His-tag on Sec31 (NHis-Sec31) still permits viability in yeast, but not in combination with other mutations targeting PRD interactions (Stancheva et al., 2020).

Several COPII ancillary proteins also possess PRDs that bind Sec23 in a similar way to Sec31, possibly stabilising the coat for formation of larger carriers during procollagen transport (Hutchings and Zanetti, 2019; Ma and Goldberg, 2016; Saito et al., 2009; Santos et al., 2016). To better understand precisely how such regulatory proteins might exert their influence, a detailed picture of the interactions within the COPII coat and their relative contributions to membrane curvature is needed.

We have previously used cryo-electron tomography (cryo-ET) and subtomogram averaging (STA) of COPII on tubulated GUVs to assess aspects of membrane-assembled coat architecture. We were able to dissect a subset of the interactions that mediate formation of the coat network, and proposed a role for the polyproline motifs in coat assembly (Hutchings et al., 2018; Zanetti et al., 2013). Here, we sought to obtain the complete picture of a fully assembled wild-type coat, aiming to visualise all interactions, and assessing their contribution to COPII function. We structurally characterize known interactions to unprecedented detail, and describe novel ones, including a charged interaction between inner and outer coat layer that was recently identified through biochemical and genetic analysis (Stancheva et al., 2020); a flexible loop on Sec23 that becomes ordered to contribute to inner coat lattice formation; and an unexpected interaction between Sec31 β-propeller and α-solenoid domains. Moreover, we discover an essential role for the structurally and functionally elusive Sec31 CTD as a key node of the COPII network.

Results

Subtomogram averaging of inner and outer coat layers

Previous X-ray crystallography and cryo-electron microscopy studies have provided partial structural insight into COPII assembly. We have high-resolution detail on some of the coat interfaces (Bi et al., 2007; Hutchings et al., 2018; Ma and Goldberg, 2016), and a low-resolution view of coat architecture (Stagg et al., 2008; Zanetti et al., 2013). However, detailed insight into the full network of interactions that mediate COPII assembly is lacking. We reconstituted budding *in vitro* by incubating purified wild type COPII components with GUVs in the presence of a non-hydrolysable GTP analogue (GMP-PNP), and visualised coated membranes by cryo-EM. As seen previously, we obtained extensive membrane remodelling, with the majority of budded membranes forming straight tubules, less frequent spherical vesicles and irregular profiles (Supplementary Fig 1A).

We collected and reconstructed high-resolution cryo-tomograms of COPII-induced tubules, which had varying diameters and were clearly coated with inner and outer coat layers (Fig. 1A,B and Supplementary Fig 1B). The inner layer arranged in a regular tightly packed lattice, while the outer layer formed a loose lozenge pattern, similar to previous reports (Hutchings et al., 2018; Zanetti et al., 2013). We used subtomogram averaging to obtain the positions and orientations of inner coat lattice units, following previously established protocols (Hutchings et al., 2018). To target the sparser outer coat lattice, we developed an unbiased, localisation-based approach (Methods and Supplementary Fig 1C,D), and obtained an average of the outer coat vertices (Fig 1C). The outer coat rhomboidal pseudo-helical lattice can be visualised by plotting neighbouring particles for each vertex (Supplementary Fig 1E, left panel). To assess the relative positioning of the two coat layers, we analysed the localisation of inner coat subunits with respect to each outer coat vertex: for each aligned vertex particle, we superimposed the positions of all inner coat particles at close range, obtaining the average distribution of neighbouring inner coat subunits. From this 'neighbour plot' we did not detect any pattern, indicating random relative positions. This is consistent with a flexible linkage between the two layers that allows adaptation of the two lattices to different curvatures (Supplementary Fig 1E).

Detailed architecture of outer coat vertices

The outer coat vertex was refined to a resolution of approximately ~12 Å, revealing unprecedented detail of the molecular interactions between Sec31 molecules (Supplementary Fig 2A). Four Sec31 N-terminal β-propeller domains interact to form 2-fold symmetric X-shaped vertices. In our subtomogram average we could clearly distinguish the β-propeller shapes and unambiguously rigid-body fit the available crystal structures into the density (Fig. 1C). The Sec13 β-propeller is also clearly defined, although features gradually degrade along rods further from the vertex, probably due to a higher degree of flexibility.

Each Sec31 β-propeller forms a different set of interactions with its neighbours, inducing a significant deviation from 4-fold symmetry. The arrangement of the Sec31 N-terminal β-propellers in our structure differs dramatically from previously published cryo-EM single particle reconstructions of outer coat vertices obtained from human Sec13-31 cages assembled in the absence of a membrane (Noble et al., 2013; Stagg et al., 2006, 2008) (Fig 1D). Indeed, when comparing the soluble cage vertex with that obtained in this study by overlapping one of the Sec31 β-propeller subunits, we find that the relative position of both neighbours is shifted by more than 15Å (Fig. 1E). In the soluble cages, a pair of opposite β-propellers in the vertex forms a tight interaction (identifying the '+' contacts (Stagg et al., 2006)), while the other pair is further apart, separated by the '+' rods (and referred to as the '-' interaction) (Fig. 1D). In the context of the membrane-assembled coat we see a clear gap between both the '+' and '-' pairs of β-propellers (Fig. 1D). Multiple effects might cause this difference: 1. Interactions of vertices arranged in a tubular geometry may be different from those on spherical vesicles; 2. Interactions in soluble cages may be distinct from those in the membrane-assembled coat; and 3. Proteins from different species may have evolved different interaction interfaces, while maintaining an overall similar

assembly architecture. We tested the first two hypotheses by examining the small populations of spherical vesicles and empty cages that were present in our tomograms. We manually picked vertices and performed carefully controlled alignments. In both cases, we detected a similar interface as in the membrane-assembled tubules, with a clear gap at the centre of the vertex despite the lower resolution (Supplementary Fig 3). While we cannot exclude that the difference we see between empty cages in our sample and those previously published might be caused by buffer conditions, it is intriguing to hypothesise that vertex interactions have evolved differently from yeast to human.

Close analysis of the β-propeller interfaces identified a region of density that likely corresponds to a negatively charged loop (residues 339-357: EQETETKQQESETDFWNNV) that is disordered in the crystal structure. Because we see density in our map, it appears that this loop becomes ordered in the assembled vertex and forms an interaction interface with the neighbouring subunits (Supplementary Fig. 4A). The proximity of this loop to the N-terminus of Sec31 might explain the vertex destabilization we observed with a N-His tag on Sec31 (Hutchings et al., 2018), which might displace or interfere with this interaction surface.

In vitro reconstitution of vesicle formation from yeast microsomal membranes using Nhis-Sec31 had previously shown that stable vertex interactions are dispensable in reactions stabilised by non-hydrolysable GTP analogues, but become necessary when coat turnover is permitted with GTP (Hutchings et al., 2018). We asked whether we could perturb the system even further and remove the Sec31 N-terminal β-propeller domain, thereby abrogating outer coat vertex interactions completely. We made a Sec31 mutant with a deletion of residues 1-372 (Sec31-ΔNTD), which did not support vesicle formation from microsomes, even with GMPPNP (Supplementary Fig 4C), and was not viable in yeast (Supplementary Fig 4D). Surprisingly, this mutant was capable of tubulating GUVs, suggesting its ability to organize the inner coat array was intact, and that inner coat organization is sufficient to drive membrane curvature of a synthetic model membrane. We propose that remodelling of cargo-containing membranes that resist budding instead requires the stable association of vertex interfaces, as well as inner coat stability tuned by GTPase activity.

Detailed structure of interconnecting rods

Outer coat vertices are connected by Sec13-31 rods that wrap tubules either in a left- or right-handed manner (Zanetti et al., 2013). As mentioned above, when refining by alignment of vertices, the density further from the centre gradually degrades, due to increased flexibility or heterogeneity. We therefore analysed the structure of the interconnecting rods by focusing the refinements at the mid-points between vertices (see Methods).

Left-handed rods (Fig 2A) averaged to a resolution of ~11 Å (Supplementary Fig 2A), and we could fit the available crystal structures of dimeric edge elements (Fath et al., 2007) by treating each monomer as a rigid body (Fig 2B,C). At this resolution we can distinguish helical profiles and individual blades of the Sec13 β-propeller (Fig 2C). As previously reported, rods in membrane-coated tubules are only slightly bent, resembling the X-ray structure (Fath et al., 2007) rather than the highly bent edges of soluble assembled cages (Fig 2B, bottom panel, Stagg et al., 2006). Surprisingly, we detected a previously unresolved extra density attached to the rod halfway between Sec13 and the dimerization interface (Fig 2B,D). The size of this appendage is indicative of a full domain. This extra density is probably sub-stoichiometric, as we could see it clearly only at low contour levels (Fig 2B,D) or in averages with lower sharpening levels (not shown). We reasoned that it could correspond to the Sec31 CTD, which is predicted to be a structured helical domain (Dokudovskaya et al., 2006; Fath et al., 2007, Supplementary Fig. 5A).

Sec31 C-terminal domain mediates essential coat interactions

To confirm that the appendage density corresponds to the CTD of Sec31 we analysed GUVs budded with a truncated form of Sec31 by cryo-EM (encompassing residues 1 to 1114, referred to as Sec31-ΔCTD, Fig. 3A,B). Inspecting cryo-tomograms of these tubules revealed no lozenge pattern for the outer

coat, whilst maintaining the typical pseudo-helical inner coat lattice (Fig. 3B). In support of a disordered outer coat lattice, our STA-based search method used for the wild-type data failed to detect vertices or long-range order for Sec31-ΔCTD (Fig. 3C). To conduct an unbiased search for rods, we repeated this search method using a featureless rod-like structure as a template, and subsequently aligned them to the subtomogram average obtained from the wild type sample. The average of Sec31-ΔCTD rods recovers the characteristic features and has similar resolution to the wild type rod, but it lacks the appendage density (Fig. 3D, orange arrowhead), unambiguously confirming this density corresponds to the CTD. The Sec31-ΔCTD rod also showed weaker density for vertices and the inner coat and membrane layer (Fig. 3D, red, blue and beige arrowheads, respectively), indicative of its disordered arrangement.

Since no atomic model for Sec31 CTD has been determined, we built an homology model to fit into the appendage density. Steroid Receptor RNA Activator protein (SRA1) is the closest homologue to Sec31 CTD for which an atomic structure exists (Bilinovich et al., 2014). SRA1 is a functionally unrelated protein that is found only in mammals, and its evolutionary links with Sec31 are unclear. Nevertheless, SRA1 and Sec31 CTD belong to the same evolutionary family and their similarity justifies the use of the SRA1 structure to build an homology model of the Sec31 CTD (see Methods). Rigid-body fitting the homology model in the appendage density shows consistency of features, and provides insights into the binding orientation of the CTD, although at this resolution we cannot determine the precise molecular interface (Supplementary Fig 5B).

In order to assess the physiological importance of the Sec31 CTD in the secretory pathway, we made yeast mutants where Sec31 was substituted with Sec31-ΔCTD. When the truncated form was the sole copy of Sec31 in yeast, cells were not viable, indicating that the novel interaction we detect is essential for COPII coat function (Fig 3E, left panel). In contrast, when the cargo burden was decreased by deletion of the ER export receptor, Emp24, Sec31-ΔCTD supported viability (Fig. 3E, right panel). We have previously interpreted this genetic rescue as evidence that bulky lumenal cargo represents a barrier to membrane curvature imposed by the coat. When such cargo are depleted from vesicles, the coat can deform the membrane with less rigidity, for example in the absence of Sec13 to rigidify the outer coat rods (Čopič et al., 2012). We hypothesise that the Sec31 CTD binding to Sec31 rods stabilises the COPII interaction network, thereby imparting rigidity and strengthening the coat. Microsome budding reconstitution experiments using Sec31-ΔCTD give further insight into this functional defect. The mutant protein is capable of forming vesicles in the presence of a non-hydrolysable GTP analogue, albeit with reduced efficiency compared to wild type. However, when GTP is used, vesicles fail to form despite Sec31-ΔCTD being efficiently recruited to membranes (Supplementary Fig. 5C,D). This indicates that CTD-mediated outer coat stabilisation becomes necessary when inner coat turnover is allowed, reminiscent of the phenotype seen with Nhis-Sec31 (Hutchings et al., 2018).

Interactions between β-propeller and α-solenoid domains define extra rod connections.

We next analysed rods that interconnect vertices in the right-handed direction (Fig 4A). Surprisingly, in addition to the CTD appendages, a second region of ill-defined extra density was present near the Sec31 dimerization region (Supplementary Fig 6A). Upon classification we could divide the right-handed rod dataset into two classes, both of which converged to resolutions between 13 Å and 15 Å (Fig. 4B and Supplementary Fig. 2A). The first class is analogous to the left-handed rods, whereas the second class has a density attached to the centre of the rod which clearly resembles a pair of β-propeller subunits, suggesting the presence of an unexpected additional Sec13-31 edge attached to the Sec31 α-solenoid. We confirmed the nature of the extra density by focussing refinements on the predicted centre of the 'extra' rod, obtaining the unambiguous shape of a Sec13-31 heterotetramer (Supplementary Fig 6B), which runs nearly perpendicular to, and bridges between, two right-handed rods. Analysis of the averages placed in the context of individual tomograms shows that the extra rods are sparsely and randomly distributed (Fig 4C) and follow a similar direction to the left-handed ones, running along the direction of the main Sec23-Sec23 inner coat interfaces (Fig 4D).

240 Since the extra rods bridge between α-solenoid dimerization interfaces of right-handed rods, we expect
241 that the distribution of neighbouring vertices compared to the centres of the extra rods should form a
242 rhombus (dotted lines in Supplementary Fig 6C). However, when we plotted the position of vertices
243 neighbouring the extra rods, we noticed that in addition to the expected peaks, there was a cluster of
244 vertices positioned in correspondence of the tip of the extra rods (Supplementary Fig 6C, red circle).
245 This suggested that a subpopulation of these extra rods could connect to a right-handed rod on one
246 side and form a standard vertex on the other. By selecting these rods and calculating their average, we
247 confirmed the presence of the two different connections (Supplementary Fig 6D). The localisation of
248 these hybrid rods in the tomogram shows that these are often placed at the interface between two
249 patches of outer coat lattice that come together with a mismatch (Supplementary Fig 6E). This indicates
250 that the novel mode of interaction we characterise here helps the outer coat network adapt to different
251 curvatures.

252 *Extended interactions between the inner coat and the Sec31 disordered region.*

253 We have shown that when outer coat polymerisation is destabilised by an N-terminal his tag on Sec31,
254 or by the lack of the CTD, vesicle formation from microsomal membranes becomes dependent on a
255 non-hydrolysable GTP analogue. Prolonged GTP binding inhibits inner coat disassembly, thereby
256 conferring functionality to a weaker outer coat (Hutchings et al., 2018). This suggests that outer coat
257 organisation in an ordered lattice contributes to the stability of the whole coat, including the inner
258 layer. To detect changes to the inner-outer coat interfaces compared with those formed with the
259 partially disrupted coat, we refined the structure of the inner coat from fully ordered coated tubules to
260 an average resolution of 4.6Å (Supplementary Fig. 2B). Density modification (Terwilliger et al., 2020)
261 and sharpening further improved features in the map (Supplementary Fig. 7A). In our previous work we
262 fit the crystal structure of inner coat components in our subtomogram averaging maps by treating them
263 as rigid bodies (Hutchings et al., 2018). The higher resolution and overall quality of our current map
264 allowed us to build regions that were missing from the X-ray structure and refine the model
265 (Supplementary Fig 7B,C). We analysed the sites of interaction with the outer coat by identifying regions
266 in the map that are not explained by the model (Fig. 5A,B). These are generally better defined than in
267 our previous map (Hutchings et al., 2018), possibly due to more stable interactions and lower flexibility.
268 We confirmed the binding of the Sec31 active region to Sec23 through its WN residues, as well as that
269 of Sec31 PPP motifs to the Sec23 gelsolin domain. Here we can clearly detect a single density that
270 extends on both sides of the prolines to contact two adjacent inner coat subunits, supporting previous
271 hypotheses that PPP-containing sequences bridge between neighbouring inner coat subunits and
272 contribute to the stability of the lattice (Fig 5B) (Hutchings et al., 2018; Ma and Goldberg, 2016;
273 Stancheva et al., 2020)).

274 In addition to the expected Sec31 binding sites, the difference map showed a prominent region that
275 we did not see in the context of Nhis-Sec31. We now see density corresponding to a long 'sausage-like'
276 region nestled in a concave surface between the Sec23 Zn-finger, helical, and gelsolin-like domains (Fig.
277 5B, asterisk). Coulombic potential representation shows that this region of the Sec23 surface is
278 negatively charged (Fig. 5C). In a recent report, we showed that binding between the outer and inner
279 layers of the COPII coat is mediated by multivalent interactions of the Sec31 disordered domain with
280 Sec23 (Stancheva et al., 2020). These interactions involve the previously identified catalytic and triple
281 proline regions, and in addition we discovered a charge-based interaction between the positively
282 charged Sec31 disordered domain and negatively charged Sec23. Charge reversal of the Sec23 surface
283 led to abolished recruitment of Sec13-31 and a non-functional coat (Stancheva et al., 2020). We are
284 now able to map this essential interaction and show it spans ~25 Å, corresponding to 9-10 residues.

285 *Sec23-Sar1 interactions in lattice formation*

286 Inner coat subunits assemble through a lattice interface between Sar1 and Sec23 from one protomer,
287 and Sec23 from the neighbouring protomer (Fig. 6A). Analysis with the PDBePISA web server (Krissinel
288 and Henrick, 2007), indicates this interface extends over a large surface of 910 $Å^2$, with individual

contacts expected to only partially contribute to its stability. The PPP-mediated contacts between one Sec23 gelsolin-like domain and the neighbour Sec23 Zn-finger domain are part of this extended interface. We also note residue S742 lies at the Sec23-Sec23 interface (Fig. 6A, inset). This is a known phosphorylation site that is involved in regulation of coat disassembly and vesicle fusion (Lord et al., 2011).

As part of the extended lattice interface, Sar1 contacts the neighbouring Sec23 trunk domain. We detect a prominent contribution mediated by a 17-residue loop of Sec23 (residues 201-217, KPTGPGGAASHLPNAMN, which we name L-loop, for lattice) that is not visible in the X-ray structures. Secondary structure predictions denote this region as disordered and highly prone to protein binding (Supplementary Fig. 7D). In our structure we can clearly visualise and model the L-loop in Sec23, which becomes partially ordered in its interaction with Sar1 (Fig 6B). To assess the importance of the L-loop interaction in lattice formation and membrane tubulation, we mutated the 17 residues to a stretch of 5 glycine-serine repeats and tested this mutant in GUV budding reactions. The Sec23 L-loop mutant did not lead to any significant phenotype, with straight tubes forming (Fig. 6C). This is not unexpected, due to the loop's marginal contribution to the inner coat lattice interface. Indeed, weakening the lattice interface by mutating PPP motifs does not change tube morphology either (Stancheva et al., 2020). However, when we aggravated the disruption by combining the Sec23 L-loop mutant with Sec31 lacking all PPPs (Sec31 ΔPPP), budding reactions showed a striking absence of straight tubules, and enrichment of multibudded profiles (Fig. 6D). This indicated that when inner coat interactions are significantly weakened, the outer coat becomes the main determinant of membrane remodelling and defaults to inducing spherical curvature. Indeed, when we also weakened outer coat vertex interactions by using an N-terminal his-tagged version of Sec31, budding gave rise to 'floppy' tubules rather than multibudded profiles (Fig. 6E).

Discussion

We have combined cryo-tomography with biochemical and genetic assays to obtain a complete picture of the assembled COPII coat at unprecedented resolution (Fig. 7). We make a number of novel observations which allow us to piece together a picture of the COPII coat as a complex network of partially redundant interactions. Structural and functional analysis of each interface reveals their role in coat assembly and membrane remodelling.

The interactions we observe between four Sec31 β-propeller subunits at the vertices of the outer coat lattice (Fig. 1) are distinct from the analogous vertices seen in human Sec31 cages assembled *in vitro* in the absence of a membrane or Sar1 (Stagg et al., 2006, 2008). The vertex structure we report here for yeast proteins is much less compact, with deviations of over 15Å in the relative positions of neighbouring β-propellers. We saw this arrangement on spherical vesicles as well as empty cages, leading us to speculate that vertex interactions have 'compacted' during evolution. As we show here and in previous work, stable outer coat vertices become important for coat function in conditions where the membrane is more difficult to deform, i.e. when inner coat turnover is allowed (Hutchings et al., 2018), or when the membranes contain cargo proteins. Indeed, deletion of the Sec31 β-propeller domain permits budding of GUVs but not from cargo-containing microsomes (Supplementary Fig. 4). It will be interesting to assess whether organisms with more complex secretory needs have selected tighter and more stable interactions at vertices.

Thorough structural analysis of the Sec13/31 rods reveals novel interactions between outer coat units. The elusive CTD of Sec31 forms a helical bundle, and its function was unknown to date. We show that Sec31 CTD is as an essential component of the outer coat network that binds to Sec31 α-solenoid domains (Fig. 2 and Supplementary Fig. 5). The Sec31 CTD is dispensable when membranes are made more deformable by depletion of certain classes of cargo, reminiscent of the role of Sec13 (Čopič et al., 2012), and suggesting that Sec31 CTD contributes to coat rigidity and/or stability. Our data paints a new picture of the assembled coat, where the outer coat C-terminal disordered region reaches down to bind and stabilise the inner coat, and then loops back to lock onto the outer coat lattice. Our data does

not distinguish between a scenario in which C-terminal domains interact in *cis* or *trans* with outer coat rods, but it is interesting to hypothesise that trans-interactions might further stabilise the coat network (Fig. 7).

We also discover a second, novel interaction within the outer coat: in addition to the known interaction of Sec31 β-propellers with each other at vertices, these domains can also bind to the Sec31 dimerisation interface, at the centre of the α-solenoid region. This leads to extra outer coat rods creating a bridge between canonical rods (Fig. 4). Occasionally these extra rods form a canonical vertex interaction at one end, and an orthogonal interaction with other rods at the other end. Such rods 'glue' mismatched patches of outer coat lattice together: they might therefore be important for outer coat stabilisation in a context of flexibility and adaptability (Supplementary Fig. 6). It is interesting that we could only detect extra rods running in the left-handed direction, and connecting canonical right-handed rods. This could be explained by the scenario in which the Sec31 disordered PRD binds to multiple Sec23 subunits in tandem, leading to preferential orientation of the extra rods with respect to the inner coat. Due to limited particle numbers, the resolution we obtained does not allow us to precisely define the residues involved in the novel interaction between the β-propeller and the α-solenoid domains of Sec31. Higher resolution will be needed to inform mutational analysis and assess the physiological and functional relevance of this novel connection.

Interactions between the outer and inner coat are mediated by Sec31 disordered PRD (Bi et al., 2007; Fath et al., 2007; Ma and Goldberg, 2016; Stancheva et al., 2020). By analysing the structure of the inner coat we confirm two interactions that have been previously defined and characterised structurally (Fig. 5): firstly, the Sec31 'active peptide' binds across Sec23 and Sar1, contributing residues in proximity to the GTP binding pocket, and accelerating Sec23 GAP activity (Bi et al., 2007). Secondly, Sec31 contains triple proline motifs, shared in metazoa by other COPII regulatory factors such as TANGO1 and cTAGE5 (Ma and Goldberg, 2016). These residues bind to the Sec23 gelsolin-like domain and appear to bridge adjacent inner coat subunits, aiding inner coat lattice formation (Hutchings et al., 2018; Ma and Goldberg, 2016). In addition, a novel, essential interaction between outer and inner coat layers was recently discovered. This is mediated by the negatively charged surface of Sec23 that was postulated to interact with positively charged clusters within the Sec31 PRD (Stancheva et al., 2020). We detect a prominent region of density bound to this region of Sec23, located within a groove formed at the junction between the gelsolin, helical and Zn-finger domains. We attribute this density to the interacting Sec31 positively charged regions (Fig. 5). Features of this extra density are less well-defined compared to the rest of the protein. Since multiple charge clusters in yeast Sec31 may contribute to this interaction interface (Stancheva et al., 2020), sequence diversity or variability at this density could explain the low resolution. Although we previously observed densities corresponding to the PPP and active peptide interactions in our structure assembled with Nhis-Sec31, the charged interaction was not detected (Hutchings et al., 2018). It is possible that ordering of the outer coat into a lattice improves the stability and occupancy of this interface.

Finally, interactions mediating inner coat assembly into a lattice are defined by our analysis. The first is the extended interface between Sec23 protomers that involves interaction with a neighbouring Sec23/Sar1 dimer (Fig. 6A). Interestingly, a known phosphorylation site, S742, is located at the Sec23-Sec23 interface. S742 has been implicated in regulating COPII turnover and ER-Golgi directionality (Lord et al., 2011). It remains to be established whether phosphorylation has any role in inner coat array assembly or disassembly. The second interface is a novel interaction between Sec23 and a neighbouring Sar1 molecule, mediated by a 17 residue loop (L-loop) in Sec23 which becomes ordered upon formation of the inner coat lattice (Fig. 6B), and whose importance in inner coat lattice assembly was confirmed biochemically.

Disrupting the inner coat lattice interface in combination with a Sec31 competent for outer coat assembly leads to budding of vesicles with spherical profiles, rather than a majority of straight tubules (Fig. 6D), indicating that outer coat assembly into cages dictates spherical membrane shape when the inner coat is unstable. This might be reflected in a physiological scenario where GTP-hydrolysis triggers

388 inner coat turnover by removing Sar1 from the membrane, favouring spherical vesicles. Metazoan
389 regulatory factors such as TANGO1 and cTAGE5, which contain PPP motifs but do not accelerate GTP
390 hydrolysis, could work by stabilising the inner coat interface while inhibiting GTP hydrolysis, favouring
391 tubules and promoting transport of large carriers such as procollagen (Ma and Goldberg, 2016). Sec23
392 is a highly conserved protein, and is present in two paralogues in metazoa: Sec23A and B. While the
393 two paralogues are thought to have largely redundant functions, mutations in Sec23A but not B cause
394 defects in secretion of procollagen (Boyadjiev et al., 2006; Fromme et al., 2007). Human Sec23A and B
395 are 85% identical, and the L-loop sequence is a region that varies significantly (Supplementary Fig. 7E).
396 Because this region is important in stabilising lattice formation, we hypothesise it is involved in
397 promoting formation of large carriers: the difference between Sec23A and B in the L-loop might confer
398 an ability to differentially support large carrier budding, and explain their distinct roles in procollagen
399 export disease.

400 We know from previous studies that partial disruption of both inner and outer coat layers is
401 incompatible with life, but can be rescued by relieving the cell of bulky cargoes (Stancheva et al., 2020).
402 Here we show that weakened coat interactions at the level of both inner and outer coat leads to the
403 formation of floppy tubules (Fig. 6E), suggesting the coat does partially assemble and impart some
404 membrane deformation, but not sufficient for active cargo transport in cells. Together, these data
405 suggest that a balance of lattice contacts between the inner and outer coats support membrane
406 budding, and this balance can be tuned to achieve different morphologies depending on membrane
407 deformability.

408 In summary, we have shown that COPII forms a complex network that assembles through partially
409 redundant interactions, whose effects are combined for a productive budding event. We have obtained
410 a detailed map of this network and have shown that the extent to which the presence and stability of
411 each interaction are necessary depends on the membrane deformability. This makes the COPII system
412 an ideal platform for regulation in response to dynamically changing cargo requirements, such as its
413 abundance, shape and size.

414 Materials and methods

415 *Cloning:*

416 Yeast COPII components were cloned from the *Saccharomyces cerevisiae* S288c genome into
417 appropriate expression vectors using In-Fusion (Takara), specifically: pETM-11 (AddGene) for Sar1 and
418 pFASTBacHTb (AddGene) for Sec23/24 and Sec13/31. N-terminal hexa-histidine purification tags were
419 cloned with an intervening TEV protease cleavage site for Sar1, Sec24 and Sec31.

420 *Protein expression and purification:*

421 Sar1

422 The pETM-11-Sar1 construct was transformed into BL21 using standard heat shock methods. Two litres
423 of BL21 were induced with 1 mM IPTG for three hours at 25°C before harvesting. Sar1 was affinity
424 purified following application to a 5 mL HisTrap colum (GE Healthcare) equilibrated in lysis/binding
425 buffer (50 mM Tris-HCl, 150 mM NaCl, 0.1% Tween-20 (v/v), 10 mM imidazole, 1 mM DTT, pH 8.0).
426 Elution was achieved with a linear gradient of elution buffer (as for binding buffer, with 500 mM
427 imidazole). Pure fractions were pooled and incubated with TEV protease at a 1:50 ratio of protease:Sar1
428 (w/w) in a sealed 10 kDa MWCO dialysis tube submerged in two litres of HisTrap binding buffer for
429 overnight dialysis at 4°C. The dialysed product was reapplied to the HisTrap column with the flow-
430 through collected and concentrated to ~0.7 mg/mL, determined using a Bradford assay.

431 Sec23/24

432 One litre of Sf9 insect cells (at $1x10^6$ cells/mL) were infected with baculovirus: 9 mL/L of untagged
433 Sec23p and 3 mL/L of His-tagged Sec24p. These were incubated for three days at 27°C and 100 rpm

434 shaking. Cells were harvested using a glass homogeniser and centrifuged at 167,424 g for one hour at
435 4°C. Sec23/24 was affinity purified following application to a 5 mL HisTrap column (GE Healthcare)
436 equilibrated in lysis/binding buffer (20 mM HEPES (pH 8.0), 250 mM sorbitol, 500 mM potassium
437 acetate, 10 mM imidazole, 10% glycerol and 1 mM DTT). Elution was achieved with a linear gradient of
438 elution buffer (as for binding buffer, with 500 mM imidazole). Pure fractions were collected and diluted
439 approximately two-fold with low salt anion-exchange binding buffer (20 mM Tris, 1 mM magnesium
440 acetate, 0.1 mM EGTA, and 1 mM DTT, pH 7.5) before application to an equilibrated 5 mL HiTrap Q
441 column (GE Healthcare). Elution was achieved with a linear gradient of elution buffer (as for binding
442 buffer, with 1 M NaCl). Pure fractions were pooled and diluted to ~1.26 mg/mL with low salt buffer and
443 10% glycerol, which were then aliquoted, flash-frozen and stored at -80°C. The same protocol was
444 applied for the Sec23 L-loop mutant. For Sec23-ΔL, residues 201-218 were mutated to 5xGS repeats
445 using Sec23 pFastBacHTb as the template. The mutation was amplified by PCR and incorporated using
446 InFusion. The same protein expression and purifcation protocol as WT Sec23/24 was used.

447 Sec13/31

448 One litre of Sf9 insect cells (at $1x10^6$ cells/mL) were infected with baculovirus: 9 mL/L of untagged
449 Sec13p and 3 mL/L of His-tagged Sec31p. To obtain His-tagged Sec13/31 (Sec13/31-NHis), the same
450 cell lysis and purification protocol (including buffers) was followed as for Sec23/24. Pure fractions from
451 anion exchange were pooled and concentrated to approximately 2 mg/mL for 50 μL aliquots, which
452 were flash-frozen and stored at -80°C.

453 For cleaved Sec13/31p an additional overnight TEV protease cleavage step was performed for His-tag
454 removal prior to anion-exchange. Following the initial affinity purification with a 5 mL HisTrap column
455 (GE Healthcare), the pooled eluate was incubated with TEV protease at a 1:50 ratio of
456 protease:Sec13/31 (w/w) in a sealed 10 kDa MWCO dialysis tube submerged in two litres of HisTrap
457 binding buffer for overnight dialysis at 4°C. The dialysed product was reapplied to the HisTrap column,
458 the flow-through was collected, and then diluted approximately fourfold with low salt buffer for
459 application to a 5 mL HiTrap Q column. Elution was achieved with a linear gradient of elution buffer
460 (same as Sec23/24 Q elution buffer). Pure fractions were pooled and concentrated to approximately 2
461 mg/mL for 50 μL aliquots, which were flash-frozen and stored at -80°C.

462 On the day of GUV BR preparation, Sec13/31 and/or NHis-Sec13/31 aliquots were thawed and gel-
463 filtrated on a 2.4 mL Superdex200 column (GE Healthcare) moutned on a ÄktaMicro (GE Healthcare)
464 system, equilibrated in HKM buffer (20 mM HEPES, 50 mM KOAc and 1.2 mM MgCl2, pH 6.8). Cleaved
465 and uncleaved versions of the Sec13/31 mutants used in this study were prepared in the same as the
466 wild-type protocol detailed above.

467 For the Sec13/31-ΔNTD, a C-terminally His-tagged version of Sec31 truncated at position 373 was used.
468 This was derived from the Sec31-NHis pFASTBacHTb construct using InFusion cloning. For the Sec13/31-
469 ΔCTD, a N-terminally His-tagged version of Sec31 covering residues 1-1114 was used. This was derived
470 from the Sec31-NHis pFASTBacHTb construct using InFusion cloning. For Sec13/31-ΔPPP, a synthetic
471 DNA construct with seven PPP to SGS mutants (853-855, 965-967, 966-968, 981-983, 1042-1044, 1096-
472 1098 and 1107-1109) was inserted into the Sec31-NHis pFASTBacHTb construct using InFusion.

473 GUV budding reactions:

474 Giant unilamellar vesicles (GUVs) were prepared by electroformation (Angelova and Dimitrov, 1986)
475 from 10 mg/mL of the "major-minor" lipid mixture (Matsuoka et al., 1998b) suspended in a 2:1
476 chloroform:methanol solvent mix, as described previously (Hutchings et al., 2018). The mixture is
477 spread over two Indium Tin Oxide (ITO)-coated glass slides, which are sandwiched with a silicon spacer
478 to create a chamber that is then filled with 300 mM sucrose. An alternating voltage of 10 Hz and 3 V
479 (rms) was applied for 6-8 hours using copper tape attached to the ITO-coated slides. GUVs were
480 harvested by gentle aspiration from the chamber and applied to 500 μL of 300 mM glucose for gravity
481 sedimentation overnight at 4°C. The supernatant was carefully aspirated and discarded to leave a ~30-
482 50 μL GUV pellet the next day. GUVs were used within two days of harvesting.

483 For GUV budding reactions (BRs), COPII proteins were incubated at defined concentrations (1 µM
484 Sar1p, 320 nM Sec23/24p, 173 nM Sec13/31p) with 1 mM GMP-PMP (Sigma-Aldrich), 2.5 mM EDTA
485 (pH 8.0) and 10% GUVs (v/v). The same concentrations were used for BRs with mutant COPII
486 components. Reactions were left at room temperature for 1-3 hours prior to negative stain or
487 vitrification.

488 *Yeast strains and plasmids:*

489 Yeast strains and plasmids used in this study were all generated using standard molecular biology
490 techniques. The yeast strains used were previously published: LMY1249 (*sec31::NAT pep4::TRP ade2-1*
491 *his3-11 leu2-3,112 + [pYCp50::SEC31-URA3])* described (Hutchings et al., 2018) and VSY015 (*sec31::NAT*
492 *emp24::KANMX pep4::TRP ade2-1 his3-11 leu2-3,112 + [pYCp50::SEC31-URA3])* described (Stancheva
493 et al., 2020). Plasmids were introduced into yeast using standard LiAc transformation methods. Cultures
494 were grown at 30°C in standard rich medium (YPD: 1% yeast extract, 2% peptone, and 2% glucose) or
495 synthetic complete medium (SC: 0.67% yeast nitrogen base and 2% glucose supplemented with amino
496 acids) as required. For testing viability, strains were grown to saturation in SC medium selecting for the
497 mutant plasmid overnight at 30°C. 10-fold serial dilutions were made in 96 well trays before spotting
498 onto 5FOA plates (1.675% yeast nitrogen base, 0.08% CSM, 2% glucose, 2% agar, 0.1% 5-fluoroorotic
499 acid). Plates were scanned at day 2 or day 3 after spotting and growth at 30°C. The *SEC31* WT plasmid
500 used in this study (VSB49) was described (Stancheva et al., 2020) and consists of *SEC31* PCR-amplified
501 with native 500 bp upstream and downstream of the gene and cloned in BamHI/NotI sites of pRS313
502 (*HIS, CEN*; (Sikorski and Hieter, 1989)). Truncations were introduced by site-directed mutagenesis using
503 the QuikChange system (Agilent) and Gibson Assembly (New England Biolabs) as per manufacturers'
504 instructions to generate VSB146 (stop codon at position 1114) and VSB131 (deletion of Val2-Gln372).

505 *Liposome binding:*

506 Liposome binding experiments were performed as described (Miller et al., 2002). Briefly, synthetic
507 liposomes of "major/minor" composition (50 mol% phosphatidylcholine, 21 mol%
508 phosphatidylethanolamine, 8 mol% phosphatidylerine, 5 mol% phosphatidic acid, 9 mol%
509 phosphatidylinositol, 2.2 mol% phosphatidylinositol-4-phosphate, 0.8% mol% phosphatidylinositol-4,5-
510 bisphosphate, 2 mol% cytidine-diphosphate-diacylglycerol, supplemented with 2 mol% TexasRed-
511 phosphatidylethanolamine and 20% (w/w) ergosterol) were dried to a lipid film in a rotary evaporator
512 and rehydrated in HKM buffer (20mM HEPES pH 7.0, 160mM KOAc, 1mM $MgCl_2$). The lipid suspension
513 was extruded 17 times through a polycarbonate filter of 0.4 µm pore size. Purified COPII components
514 and lipids were mixed to final concentrations of 0.27mM liposomes, 15µg/ml Sar1, 20µg/ml
515 Sec23/Sec24, 30µg/ml Sec13/Sec31 and 0.1mM nucleotide in 75µl HKM Buffer. Binding reactions were
516 incubated for 30 min at 25°C. Each sample was mixed with 50µl 2.5M Sucrose-HKM, then 100µL
517 transferred to a ultracentrifuge tube, overlaid with 100µl 0.75M Sucrose-HKM and 20µl HKM. The
518 gradients were spun (100 000 rpm, 25 min, 24°C with slow acceleration/deceleration) in a Beckman
519 TLA-100 rotor. The top 30µl of the gradients were collected and normalised for lipid recovery using
520 Typhoon FLA 7000 scanner (GE). Samples were then resolved by SDS-PAGE and visualised using SYPRO
521 Red staining.

522 *Microsome budding assays:*

523 Microsomal membranes were prepared from yeast as described (Wuestehube and Schekman, 1992).
524 Briefly, yeast cells were grown to mid-log phase in YPD (1% yeast extract, 2% peptone, and 2% glucose),
525 harvested and resuspended in 100mM Tris pH 9.4/10mM DTT to 40 OD_{600}/ml, then incubated at room
526 temperature for 10 min. Cells were collected by centrifugation and resuspended to 40 OD_{600}/ml in
527 lyticase buffer (0.7M sorbitol, 0.75X YPD, 10mM Tris pH 7.4, 1mM DTT + lyticase 2µL/OD_{600}), then
528 incubated at 30ºC for 30 min with gentle agitation. Cells were collected by centrifugation, washed once
529 with 2X JR buffer (0.4M sorbitol, 100mM KOAc, 4mM EDTA, 40mM HEPES pH 7.4) at 100 OD_{600}/ml, then

530 resuspended in 2X JR buffer at 400 OD_{600}/ml prior to freezing at -80ºC. Spheroplasts were thawed on
531 ice, and an equal volume of ice cold dH20 added prior to disruption with a motor-driven Potter Elvehjem
532 homogenizer at 4ºC. The homogenate was cleared by low speed centrifugation and crude membranes
533 collected by centrifugation of the low-speed supernatant at 27,000 x g. The membrane pellet was
534 resuspended in ~6mL of buffer B88 (20mM HEPES pH 6.8, 250mM sorbitol, 150mM KOAc, 5mM
535 $Mg(OAc)_2$) and loaded onto a step sucrose gradient composed of 1mL 1.5M sucrose in B88 and 1mL
536 1.2M sucrose in B88. Gradients were subjected to ultracentrifugation at 190,000 x g for 1h at 4ºC.
537 Microsomal membranes were collected from the 1.2M/1.5M sucrose interface, diluted 10-fold in B88
538 and collected by centrifugation at 27,000 x g. The microsomal pellet was resuspended in a small volume
539 of B88 and aliquoted in 1mg total protein aliquots until use.

540 Budding reactions were performed as described (Miller et al., 2002). Briefly, 1mg of microsomal
541 membranes per 6-8 reactions was washed 3x with 2.5 M urea in B88 and 3x with B88. Budding reactions
542 were set up in B88 to a final volume of 250 µl at the following concentrations: 10µg/µl Sar1, 10µg/µl
543 Sec23/Sec24, 20µg/µl Sec13/Sec31 and 0.1mM nucleotide. Where appropriate, an ATP regeneration
544 mix was included (final concentration 1mM ATP, 50µM GDP-mannose, 40mM creatine phosphate,
545 200µg/ml creatine phosphokinase). Reactions were incubated for 30 min at 25°C and a 12 µl aliquot
546 collected as the total fraction. The vesicle-containing supernatant was collected after pelleting the
547 donor membrane (15 000 rpm, 2 min, 4°C). Vesicle fractions were then collected by centrifugation in a
548 Beckman TLA-55 rotor (50 000 rpm, 25 min, 4°C). The supernatant was aspirated, the pelleted vesicles
549 resuspended in SDS sample buffer and heated for 10 min at 55°C with mixing. The samples were then
550 analysed by SDS-PAGE and immunoblotting for Sec22 (Miller lab antibody) and Erv46 (a gift from
551 Charles Barlowe).

552 *EM sample preparation:*

553 For cryo-electron tomography:

554 4 µL of the GUV COPII BR was applied to negatively glow-discharged C-flat holey carbon coated gold
555 grids (CF-4/1-4AU, Electron Microscopy Sciences), blotted from both sides (60 seconds pre-blot wait,
556 blot force setting five, and four second blot time) and plunge-frozen in 100% liquid ethane on a Vitrobot
557 Mark IV (FEI) set to 4°C and 100% humidity. 3 µL of BSA-blocked 5 nm gold nanoparticles (BBI Solutions)
558 were added to a 30 µL GUV BR and gently agitated just prior to vitrification. Vitrified grids were stored
559 in liquid nitrogen dewars to await data collection.

560 For negative stain:

561 4 µL of the GUV COPII BR was applied to negatively glow-discharged grids (Carbon film 300 Copper
562 mesh, CF300-Cu), stained with 2% uranyl acetate, blotted with filter paper and air-dried at room
563 temperature. Grids were imaged using either a Tecnai 120 keV TEM (T12) fitted with a CCD camera, or
564 a Tecnai 200 keV TEM (F20) fitted with a DE20 detector (Direct Electron, San Diego). Unaligned and
565 summed frames were collected for F20 images with a dose of 20-30 e^-/pixel/second.

566 *Cryo-electron tomography data collection:*

567 For wild-type COPII GUV BRs, a total of 286 dose-symmetric tilt series (Sikorski and Hieter, 1989) with
568 +/- 60° tilt range and 3° increments were acquired on Titan Krios operated at 300 keV in EFTEM mode
569 with a Gatan Quantum energy filter (20 eV slit width) and K2 Summit direct electron detector (Gatan,
570 Pleasanton CA) at ~1.33 Å/pixel. Data were collected at the ISMB EM facility in Birkbeck College and at
571 the Cryo-EM Service Platform at EMBL Heidelberg. For ΔCTD-Sec31, 47 dose-symmetric tilt series were
572 collected at Birkbeck with a K3 direct detector (Gatan, Pleasanton CA) at ~ 1.38 Å/pixel. For all sessions,
573 defocus was systematically varied between 1.5 and 4.5 µm (Table 1). Data was collected automatically
574 using SerialEM (Mastronarde, 2005) after manually selecting tubes using the AnchorMap procedure.
575 Dose per tilt varied between 2.9 and 3.7 $e^-/Å^2$, equating to ~120 and ~150 $e^-/Å^2$ in total respectively,
576 depending on the dataset (Table 1).

Cryo-tomography data processing:

Tilt frames from Birkbeck were aligned using whole frame alignment with MotionCor2 (Zheng et al., 2017), which were amalgamated into ordered stacks. Tilt series were either aligned manually with IMOD or automatically with the Dynamo tilt series alignment (*dtsa*) pipeline (Castaño-Díez et al., 2012). Weighted back-projection (WBP) was used to reconstruct bin8x tomograms with 50 iterations of SIRT-like filtering for initial particle-picking and STA. CTF estimation was performed with CTFFIND4 on a central rectangular region of the aligned and unbinned tilt series, as done previously (Hutchings et al., 2018). The uncropped, aligned and unbinned tilt series were dose-weighted using critical exposure values determined previously using custom MATLAB scripts (Grant and Grigorieff, 2015). 3D-CTF correction and tomogram reconstruction was performed using the novaCTF pipeline (Turoňová et al., 2017), with bin2x, bin4x and bin8x versions calculated using IMOD *binvol* (Kremer et al., 1996).

Subtomogram averaging:

All STA and subsequent analysis was performed using a combination of Dynamo (Castaño-Díez et al., 2012) and custom MATLAB scripts.

Inner coat:

Initial particle-picking for the inner coat was performed using previously established protocols (Hutchings et al., 2018; Zanetti et al., 2013). Briefly, tube axes were manually traced in IMOD to generate an oversampled lattice of cylindrical surface positions with angles assigned normal to the surface. 32^3 voxel boxes were extracted from bin8x SIRT-like filtered tomograms for one round of initial reference-based alignments using a resampled and 50 Å low-pass filtered version of the inner coat reconstruction EMDB-0044 (Hutchings et al., 2018). Manual inspection of geometric markers using the UCSF Chimera placeObjects plug-in (Pettersen et al., 2004; Qu et al., 2018) confirmed convergence of oversampled coordinates onto the pseudo-helical inner coat lattice.

To rid outliers from the initial alignments, three strategies were used. Firstly, distance-based cleaning was applied using the Dynamo "separation in tomogram" parameter, set to four pixels. This avoids duplication of data points by identifying clusters of converged particles and selecting the one with the highest cross-correlation (CC) score. Secondly, particles were cleaned based on lattice directionality. Initial alignments were conducted on a tube-by-tube basis using the Dynamo in-plane flip setting. Particles not conforming to the major directionality were discarded by using the Dynamo *dtgrep_direction* command in custom MATLAB scripts. Thirdly, manual CC-based thresholding was implemented to discard misaligned particles. As seen previously (Hutchings et al., 2018), particles on the tubule surface exhibited an orientation-dependent (Euler angle θ) CC score whereby top and bottom views had lower CC values. These were reweighted using the same polynomial fit for θ versus CC (MATLAB fit with option 'poly2') as described previously for more convenient thresholding. The cleaned initial coordinates were then combined and divided into half datasets for independent processing thereon.

Subsequent STA progressed through successive binning scales of 3DCTF-corrected tomograms, from bin8x to 4x, 2x then unbinned. At each level, angular and translational searches were reduced, with the low-pass filter determined by the Fourier shell correlation (FSC) 0.5 cut-off between the two half-maps. A saddle-shaped mask mimicking the curvature of the membrane at the height of the inner coat layer was used throughout. A total of 151,176 particles contributed to the map.

Half maps were used for density modification using Phenix (Terwilliger et al., 2020). The same mask used for alignments was imposed, and the density modification procedure was carried out without reducing the box size. All other parameters were used as default. After density modification, the map was further sharpened using the 'autosharpen' option in Phenix (Liebschner et al., 2019).

Outer coat:

Oversampled coordinates for the outer coat were obtained by radially shifting refined inner coat coordinates by eight pixels in Z, following initial alignments from SIRT-like filtered tomograms

(Supplementary Fig. 1). 64^3 voxel boxes were extracted from bin8x SIRT-like filtered tomograms for one round of initial reference-based alignments using a resampled and 50 Å low-pass filtered version of the outer coat tetrameric vertex reconstruction EMDB-2429 (Zanetti et al., 2013). Again, manual inspection of positions and orientations with the placeObject plug-in confirmed conformity to the expected lozenge-shaped outer coat lattice (Supplementary Fig. 1). Moreover, density for the neighbouring outer coat vertices emerged outside of the alignment mask and template, suggesting these initial alignments are not suffering from reference bias. The cleaned initial coordinates were then combined and divided into half datasets for independent processing thereon.

Subsequent STA progressed through successive binning scales of 3DCTF-corrected tomograms, from bin8x to 4x, to 2x, for a final pixel size of 2.654 Å. At each level, angular and translational searches were reduced, with the low-pass filter determined by the Fourier shell correlation (FSC) 0.5 cut-off between the two half-maps. A mask mimicking the curvature of the outer coat layer was used throughout. Prior to sharpening of the final unbinned map using relion 'postprocessing', the final half dataset averages were amplitude-weighted according to the sum of the combined CTFs.

The refined positions of vertices were used to extract left and right-handed rods using the dynamo sub-boxing feature. Left-handed rods were processed as vertices, except that a cylindrical mask was used during alignmnents. Right handed rods were subjected to classification in dynamo using multi-reference alignments. One class contained canonical rods, and particles belonging to this class were further processed as above. Two classes which contained the extra rod attachment were combined after applying a 180° in-plane rotation to particles in one class. After that, processing was carried out as for the other subtomograms.

The number of particles that contributed to outer coat averages is reported in Table 1.

Sec31-ΔCTD outer coat rods:

Oversampled coordinates for the outer coat were obtained in the same way as the WT dataset. Initial alignments using the previously resolved tetrameric vertex (EMDB-2429) did not produce lattice patterns conforming to the expected lozenge-shape as judged from the placeObjects inspection. This was confirmed by the subtomogram neighbour analysis for the refined initial alignment coordinates. Furthermore, the resulting average did not reveal new features emerging outside of the mask or initial reference. To confirm that Sec31-ΔCTD rods lack the appendage seen in the WT rod maps, we instead performed initial alignments against a rod without handedness. For this, the final left-handed rod from the WT dataset was taken and rigid body fitted with the crystal structure (PDB 4bzk) in UCSF Chimera (Pettersen et al., 2004) to generate a 30 Å *molmap*. This was duplicated, mirror-symmetrisez with the flipZ command in Chimera, and rotated along the axis of the rod by 180°, and summed with the original molmap using *vopMaximum* to create a Sec13/31 rod without handedness. This was used as a template for initial alignments, keeping Dynamo parameters consistent with vertex alignments at the same stage. This resulted in a rod which regained the original handedness of Sec13/31, suggesting no reference bias. To clean the dataset of misaligned particles, MRA with five classes and no shifts or rotations allowed was performed for 100 iterations. Two stable classes comprising ~90% of the data emerged as recognisable Sec13/31 rods. Refinement of each of these selected classes against a wild type left-handed rod gave averages that lacked the putative CTD appendage.

The procedure was repeated independently for two half datasets for resolution assessment.

Subtomogram neighbour analysis:

To provide a semi-quantitative readout for the degree of lattice order, neighbour plots were calculated and used in a similar way to previous STA studies (Kovtun et al., 2018, 2020). Briefly, all neighbouring particles are identified within a user-defined distance on a particle-by-particle basis. The relative orientation and distance to the matched particle is used to fill the relevant pixel in a master volume relative to its centre, which accumulates into a volume of integers. In a well ordered lattice, this results in peaks of high intensity in the master volume. The final volumes are divided by the number of searched particles and normalised to a maximum intensity of one. For convenient visualisation, pixels in Z were summed to create heatmap representations. Furthermore, this master volume retains

675 matched particle pairings, and can be masked to select specific relationships in the dataset
676 (Supplementary Fig. 6C).

677 Outer coat in spherical vesicles and cages:

678 Vesicles and cages were identified, and vertices manually picked from gaussian filtered binned x8
679 volumes using UCSF Chimera (Pettersen et al., 2004). Initial orientations were assigned normal to the
680 vesicle or cage centre, and the in plane rotation angle was randomised. Vertices were then aligned for
681 one iteration to the relevant starting reference (Supplementary Fig. 3), searching out of plane angles
682 within a cone and the full in plane rotation range.

683 *Fitting and interpretation:*

684 The map output from phenix.resolve_cryoem (Terwilliger et al., 2020) and the further sharpened map
685 were used to provide guidance for model building.

686 Crystal structures of Sec23 (2QTV), Sec24 (1PCX), Sar1 (2QTV), Tango1 (5KYW) and Sec31 active peptide
687 (2QTV) were fitted to the reconstruction using UCSF Chimera (Pettersen et al., 2004) and Coot (Emsley
688 et al., 2010).

689 Two copies of each protein were placed, representing two protomeric assemblies. Clashes between
690 Sec23 from adjacent protomers were resolved by manual rebuilding. Clear density was also observed
691 for residues 201-217 of Sec23, 363-371and 463-466 of Sec24, and 157-159 of Sar1, and were manually
692 built as they were absent from the crystal structures.

693 The model was refined with phenix.real_space_refine against the sharpened map, and validated with
694 phenix.validation_cryoem (dev 3885) (Table 3).

695 *Homology modelling:*

696 Sec31 residues 481-1273 (encompassing PRD and CTD regions) was used to search for remote
697 homologues using the HHpred server (Zimmermann et al., 2018), and identifying SRA1 as the closest
698 homologue in the PDB database (PDB 2MGX, E-value 2.3E-15). To confirm the homology, the Sec31
699 protein sequence (Uniprot id: P38968) was used to search the CATH database of functional families
700 (Sillitoe et al., 2015), generating a significant hit to a Sec31 CTD functionl family (E-value 6.0E-48). SRA1
701 matched this family with an E-value of 0.0001, which is within the threshold for homology modelling
702 using functional family matches, based on previous benchmarks (Lam et al., 2017).

703 Homology models of Sec31 CTD were built using a combination of HHpred and Modeller (Webb and
704 Sali, 2017), based on the highest-ranking homologue structure of SRA1 (Bilinovich et al., 2014).

705 *Tables:*

706 Table 1: Data collection parameters

	WT COPII (1)	WT COPII (2)	ΔCTD
Grids	C-flat holey carbon coated gold grids (CF-4/1-4AU, Electron Microscopy Sciences)	C-flat holey carbon coated gold grids (CF-4/1-4AU, Electron Microscopy Sciences)	Lacey Carbon film, 200 Copper, (S166-3, Agar Scientific)
Cryo-specimen freezing	Vitrobot Mark IV	Vitrobot Mark IV	Leica EM GP
Electron microscope	Titan Krios, EMBL	Titan Krios, Birkbeck	Titan Krios, Birkbeck
Detector	K2 direct detector, Gatan	K2 direct detector, Gatan	K3 direct detector, Gatan
Datasets	1	1	1

Micrographs (used in processing)	137 tomograms	149 tomograms	47 tomograms
Voltage (keV)	300		
GIF energy filter slit width (eV)	20		
Electron exposure ($e^-/Å^2$)	~ 120	~ 150	~ 120
Sampling interval	1.33 Å/pixel	1.327 Å/pixel	0.69 Å/pixel (superresolution), 1.38 Å/pixel 2x2 binned.
Exposure time	0.25 sec frame / 0.75 sec total	0.1 sec frame / 1 sec total	0.08 sec frame / 0.4 sec total
Defocus range	-1.5 to -4.5 µm	-1.5 to -4.5 µm	-1.5 to -3.5 µm
Defocus determination	CTFFIND4		

Table 2: 3D STA reconstructions and model refinement

	Inner coat	Outer coat			
		Vertex	Left-handed rod	Right-handed rod	Right-handed rod with extra
Particle box size	196	128	128	128	128
Number of particles used	151,176	14,099	16455	7958	7195
Initial map generation	Dynamo	Dynamo	Dynamo	Dynamo	Dynamo
Map refinement	Dynamo	Dynamo	Dynamo	Dynamo	Dynamo
Resolution	4.6 Å	12 Å	11 Å	13 Å	15 Å

Table3: refinement statistics for the inner coat

Model composition	
Protein residues	3413
No. Ligands	8
Protein atoms	26852
Ligand atoms	70
Model Resolution @ FSC 0.5 (Å)	4.7
Map CC (mask)	0.716
Average B-factor (all atoms) ($Å^2$)	158.4
RMS deviations – Bonds (Å)	0.01
RMS deviations – Angles (deg)	1.52

Molprobity Score	2.18
Clashscore	13.11
Ramachandran plot (%)	
Favoured	89.7
Allowed	10.1
Outlier	0.21
C-beta deviations (%)	0.00
Rotamer Outliers (%)	0.07

Figure Legends

Figure1. Architecture of outer COPII coat vertices

A. Slices through different z heights of a binned and filtered representative cryo-tomogram of COPII-coated tubule. Inner and outer coats (blue and red arrowheads respectively) are visible. Scale bar 50 nm.

B. Schematic representation of outer coat architecture. Sec13-31 subunits arrange in a lozenge pattern, around the inner coat that arranges in a tightly packed lattice. Panels C-E focus on the structure of vertices, boxed in this schematics.

C. 12 Å subtomogram average of the COPII vertex, with rigid-body fitted atomic models (PDB 2PM6 and 2PM9). Sec31 protomers in dark red and orange, Sec13 in gray.

D. Comparison of the vertex reconstructed from coated membrane tubules (this study), with that of cages obtained in the absence of membranes (Noble et al., 2013). The '-' protomers are in dark red, and the '+' protomers are shown in orange and blue respectively.

E. The fitted atomic models were superimposed on a '-' Sec31 protomer, and the relative positions of the neighbouring '+' protomers are overlapped, highlighting the differences between the two architectures.

Figure 2. Architecture of left-handed COPII rods

A. Schematic representation of outer coat lozenge architecture, with left-handed rod positions highlighted in the box.

B. Top panel: top view of the 11 Å subtomogram average of the COPII left-handed rod, with rigid-body fitted atomic models (PDB 2PM6). The dimerising protomers are shown in dark and light pink, Sec13 in grey. Bottom panel: sideview of B.

C. Details of the map in B, showing the quality of the fit. Left panel: detail of Sec13 β-propeller. Righ panel: detail of Sec31 α-solenoid domain.

D. Enlargement of the region boxed in panel B shown at lower contour to display an extra density.

Figure 3. Role of the Sec31 CTD

A. Domain organisation of Sec31, including the N-terminal β-propeller domain, the Sec13 insertion blade, a central α-solenoid dimerization domain, a disordered, proline-rich region, and the CTD (top). The mutant protein analysed in this figure was truncated before the CTD (bottom).

B. Slices through different z heights of a binned and filtered representative cryo-tomogram of COPII-coated tubule formed with Sec31-ΔCTD. Arrowheads as in Fig. 1A. The outer coat appears disordered. Scale bar 50 nm.

743 C. Analysis of positions of neighbouring particles for aligned vertices. In tubules formed with wild type
744 Sec31 (left panel), vertices are arranged in a lozenge pattern, while in tubules formed with Sec31-ΔCTD
745 no pattern is visible. Scale bar 50 nm.

746 D. Top panels: slices through xy and yz planes of 8X binned subtomogram average of rods extracted
747 from wild type tubules. Orange arrowheads indicate the appendage density in Fig 2D. Red arrowhead
748 indicates the vertex, and beige is the membrane. Bottom panels. The same slices for the average of
749 rods extracted from tubules formed with Sec31-ΔCTD. Extra density is absent, confirming its
750 assignment to Sec31 CTD. The density for the vertex and membrane is also fainter, indicating overall
751 disorder of rods in this sample. Scale bar 10 nm.

752 E. Left panel: a *sec31Δ* yeast strain transformed with the indicated plasmids was tested on 5-FOA,
753 revealing lethality associated with deletion of the CTD. Right panel: the same plasmids were
754 transformed into a *sec31Δ emp24Δ* yeast strain revealing rescue of viability.

755 *Figure 4. Architecture of left-handed COPII rods*

756 A. Schematic representation of coat architecture, with right-handed rod positions highlighted in the
757 box.

758 B. Top panel: top view of the 13 Å subtomogram average of the COPII right-handed rod with no extra
759 density at the dimerization interface, with rigid-body fitted atomic models (PDB 2PM9). The dimerising
760 protomers are shown in dark and light pink, Sec13 in grey. The CTD is visible in these rods. Bottom
761 panel: the same view of a class of right-handed rods that displays an attachment of another rod. The
762 Sec13-31 beta propeller tandem is fitted (Sec31 in green and Sec13 in grey).

763 C. Averages of vertices (dark red), left and right-handed rods (pink) are placed in their aligned positions
764 and orientations in a representative tomogram. Extra rods are placed in green, and display random
765 distribution, but unique orientation.

766 D. Enlargement of the placed object, with the placed inner coat (grey), showing that extra rods orient
767 roughly parallel to the inner coat lattice direction.

768 *Figure 5. Inner-outer coat interactions*

769 A. Top: the inner coat lattic structure, with a box indicating the region represented in panels B and C.
770 Bottom: schematic representation of coat architecture, with inner coat highlighted in the box.

771 B. The density-modified inner coat subtomogram average and the refined atomic model. The map is
772 coloured in transparent white, while regions that are further than 3 Å from the model are coloured in
773 dark red, indicating density that is not explained by the model and is attributed to outer coat binding.

774 C. The difference map between the map and a model-generated density (filtered at 4 Å, yellow) is
775 overlaid to the model surface coloured according to its Coulombic potential. The outer coat density
776 indicated by the asterisk binds to a negatively charged groove on Sec23.

777 *Figure 6. Interface between inner coat subunits*

778 A. The interface between neighbouring inner coat subunits viewed from the top. A dotted line defines
779 the boundary between two protomers. In the inset, the Sec23-Sec23 interface viewed from the side, in
780 the direction of the arrow. S742 is highlighted in purple.

781 B. Enlarged view of the Sec23-Sar1 interface, with the modelled Sec23 17-residue L-loop in dark cyan.
782 This loop is disordered in the X-ray structure, but becomes ordered in the lattice, mediating interactions
783 with Sar1.

784 C. GUV budding reconstitutions in the presence of wild type Sec31 and Sec23 lacking the L-loop show
785 straight tubules, similar to wild type reactions.

786 D. Budding creates spherical profiles when Sec31 has all of its PPP sites mutated to alanine to further
787 weaken inner coat assembly.

E. Floppy tubules form when, in addition to the conditions in D, Sec31 vertex interactions are destabilised with Nhis-Sec31. Scale bar 100 nm.

Figure 7. A map of the COPII coat assembly network

A model for how COPII assembles on membranes. Three sets of interactions contribute to coat assembly:

1. Outer-outer coat. Mediated by Sec31 β-propellers forming vertices, by Sec31 β-propellers binding to the α-solenoid domain of a different protomer to create 'bridging' rods, and by Sec31 CTD binding to Sec31 α-solenoid domain. It is unclear whether the latter interaction occurs in cis or trans.

2. Outer-inner coat. Mediated by Sec31 disordered region, contributing three interaction sites: triple proline motifs bind to Sec23 bridging between neighbouring subunits; the active fragment binds across Sec23 and Sar1 to accelerate GAP activity, and positively charged clusters bind to a negatively charged groove on Sec23.

3. Inner-inner coat. Mediated by Sec31 PPP motifs (see above), and by an extended lattice interface which includes Sec23-Sec23 interactions as well as Sec23-Sar1 interactions mediated by the L-loop.

Supplementary Figure 1. Overview of subtomogram averaging.

A. A typical view of GUV budding on grids. Scale bar 1um.

B. Tube diameter distribution. Average diameter is 57 +/- 5 nm.

C. Workflow for extraction of outer coat subtomograms. Top: aligned inner coat subunits arrange in a lattice. Middle: radially shifted coordinates from inner coat lattice points are used to extract outer coat particles. This oversamples the outer coat lattice. Bottom: alignments of outer coat particles with large shift in their xy plane but restricted shifts in the z direction leads to finding outer coat subunit accurately, as shown by the outer coat lattice pattern. This strategy was necessary to avoid the high-signal inner coat to bias the alignments.

D. Left panel: the starting reference is shown overlaid with the mask used. Right panel: the average obtained after one iteration clearly shows continuous density outside the mask, including neighbouring vertices and underlying smeared inner coat layer, indicative of genuine alignments.

E. Left panel: plot of the positions of neighbouring vertices to each aligned vertex shows the expected pattern. Right panel: plot of neighbouring inner coat subunits with respect to each vertex does not show any pattern, indicating the two coat layers are disordered with respect to each other. Scale bar 50 nm.

Supplementary Figure 2. Resolution of subtomogram averages.

A. Fourier Shell Correlation between independently processed half maps for the outer coat structures, colours as indicated in the legend. Line indicating FSC=0.143 is drawn.

B. Fourier Shell Correlation between independently processed half maps for the inner coat.

Supplementary Figure 3. Vertices on round vesicles and empty cages are hollow.

A. 79 vertices were manually picked from spherical vesicles, and aligned against starting references originated either from a low-pass filtered version of the vertex obtained from tubules, or to the vertex of soluble cages obtained through in vitro assembly in the absence of membranes. In both cases, averages show a hollow architecture, more similar to the vertex arrangement we see on membrane tubules. Places vertex confirm the alignments are correct.

B. As in A, but 205 vertices were manually picked from membrane-less cages that were found in the cryo-tomograms as by-products of budding reactions. Scale bar 50 nm.

Supplementary Figure 4. Vertex interaction between Sec31 N-terminal β-propellers.

831 A. A bottom view of the vertex reconstruction (outlined transparent white), with fitted models (Sec31
832 in dark red and orange, and Sec13 in grey). In the model, the N-terminal residues are highlighted in
833 blue, and the stubs of an acidic loop missing from the X-ray structures are highlighted in green. The
834 difference map between the subtomogram average and the model is shown in green, and is consistent
835 with being occupied by the acidic loop.

836 B. Negatively stained GUV budding reconstitutions with Sec31 deleted of its N-terminal β-propeller
837 domain show tubulation and ordered inner coat lattice. Scale bar 100 nm.

838 C. *In vitro* budding experiments using yeast microsomal membranes incubated with Sar1, Sec23/Sec24,
839 Sec13 with the indicated mutant of Sec31, and the indicated nucleotides. Vesicle release from the
840 donor membrane is measured by detecting incorporation of COPII cargo proteins, Sec22 and Erv46,
841 into a slowly sedimenting vesicle fraction. When the NTD of Sec31 is missing, no budding is detected.

842 D. A *sec31Δ* yeast strain transformed with the indicated plasmids was tested on 5-FOA, revealing
843 lethality associated with deletion of the NTD.

844 E. Flotation assays measure recruitment of COPII proteins to buoyant liposomes. Sec31-ΔNTD is
845 recruited with similar efficiency to wild type Sec31, indicating that the budding and viability defects are
846 not due to low recruitment levels.

847 *Supplementary Figure 5. Sec31 CTD characterisation.*

848 A. Secondary structure predictions of Sec31 CTD indicate the presence of a folded domain, consisting
849 mainly of α-helices.

850 B. A homology model for the Sec31 CTD was built based on SRA1, a mammalian homologue. The
851 homology model was fitted to the appendage density and shows consistency of features.

852 C. As in Supplementary Fig. 4C. When Sec31 CTD is missing, weak budding is detected with non-
853 hydrolisable GTP analogues but not with GTP.

854 D. As in Supplementary Fig. 4E. Sec31-ΔCTD is efficiently recruited to membranes, indicating the
855 functional defects are not a consequence of low recruitment levels.

856 *Supplementary Figure 6. Analysis of extra rods connecting between right-handed rods.*

857 A. Right handed rods after the first round of alignments (bin x 8) showed prominent extra density.

858 B. After classification, a class emerged of right-handed rods which had a structured domain attached
859 to the dimerization interface, resembling a tandem of β-propeller domains of Sec13-31 rods. Sub-
860 boxing was performed by extracting particles at the predicted centre of the extra rods, and
861 subtomogram averaging and subsequent alignments clearly converged into a Sec13-31 rod structure.

862 C. The plotted position of vertices neighbouring the extra rods. Given the extra rods position within the
863 outer coat lattice (green line), vertices are predicted to position at the corners of a rhombus (dotted
864 pink lines). An extra peak was detected in the neighbour plot, which corresponds to the tip of the extra
865 rod (red circle).

866 D. Selecting and averaging extra rod particles based on masks on the neighbour plot clearly shows that
867 some of these rods are connected to a right-handed rod on one side, and a vertex on the other.

868 E. Rods selected in D (green) were placed together with the canonical rods and vertices (dark pink and
869 red, respectively), showing that they bridge between patches of mismatched outer coat lattice.

870 *Supplementary Figure 7. Inner coat subtomogram averaging.*

871 A. Overview of the sharpened map, with the central subunit coloured according to the model.

872 B. The X-ray-based model of Sec23, Sec24 and Sar1 was refined in the map, as detailed in the methods.

873 C. A close up view of the model in the core of Sar1, showing clear separation of β-strands and density
874 for the bound nucleotide.

D. Disorder prediction of the Sec23 region around the L-loop (inset), as done with the PSIPRED server(Buchan and Jones, 2019).

E. Alignment between human Sec23A and B paralogues shows very high conservation throughout the proteins, aside of a short region corresponding to the L-loop.

Acknowledgements

We thank Euan Pyle and Natasha Lukoyanova for comments on the manuscript. We thank Natasha Lukoyanova at the ISMB Birkbeck cryo-EM lab, and Wim Hagen at the EMBL cryo-EM facility in Heidelberg for cryo-tomography data collection, Tom Terwilliger at Los Alamos National Laboratory for advice on density modification procedures, and Christine Orengo and Natalie Dawson for help with Sec31 CTD bioinformatics analysis. **Funding**: This work was supported by grants from the Academy of Medical Sciences (Springboard award SBF0031030), the ERC (StG 852915 – CRYTOCOP) and the BBSRC (BB/T002670/1) to GZ, the UK Medical Research Council (MRC_UP_1201/10) to EAM and the Wellcome Trust (102535/Z/13/Z) to ACMC. Cryo-EM data for this investigation were collected at Birkbeck College, University of London, with financial support from the Wellcome Trust (202679/Z/16/Z and 206166/Z/17/Z), and at the Cryo-EM Service Platform at EMBL Heidelberg.

Author contributions: Conceptualization: GZ, JH; Funding acquisition: GZ, EAM; **Investigation**: Sample preparation: JH, NRB; cryo-tomography data collection: JH; cryo-tomography and subtomogram averaging data processing: JH, GZ; yeast viability and microsome budding assays: VS, EAM; model building and refinement: AC. **Writing**: original draft: GZ, JH; review and editing: all authors. **Data and materials availability**: We have deposited the EM maps and models to the Electron Microscopy and Protein Data Banks with accession codes: EMD-11193,11194,11197,11198,11199 and PDB 6ZG5,6ZG6,6ZGA.

Competing interests: The authors declare no competing interests.

References

Angelova, M.I., and Dimitrov, D.S. (1986). Liposome Electro formation. Faraday Discuss. Chem. SOC *81*, 303–311.

Antonny, B., Madden, D., Hamamoto, S., Orci, L., and Schekman, R. (2001). Dynamics of the COPII coat with GTP and stable analogues. Nature Cell Biology *3*, 531–537.

Bacia, K., Futai, E., Prinz, S., Meister, A., Daum, S., Glatte, D., Briggs, J.A.G., and Schekman, R. (2011). Multibudded tubules formed by COPII on artificial liposomes. Sci Rep *1*, 17.

Barlowe, C., Orci, L., Yeung, T., Hosobuchi, M., Hamamoto, S., Salama, N., Rexach, M.F., Ravazzola, M., Amherdt, M., and Schekman, R. (1994). COPII: a membrane coat formed by Sec proteins that drive vesicle budding from the endoplasmic reticulum. Cell *77*, 895–907.

Bi, X., Corpina, R.A., and Goldberg, J. (2002). Structure of the Sec23/24-Sar1 pre-budding complex of the COPII vesicle coat. Nature *419*, 271–277.

Bi, X., Mancias, J.D., and Goldberg, J. (2007). Insights into COPII coat nucleation from the structure of Sec23.Sar1 complexed with the active fragment of Sec31. Dev. Cell *13*, 635–645.

Bilinovich, S.M., Davis, C.M., Morris, D.L., Ray, L.A., Prokop, J.W., Buchan, G.J., and Leeper, T.C. (2014). The C-Terminal Domain of SRA1p Has a Fold More Similar to PRP18 than to an RRM and Does Not Directly Bind to the SRA1 RNA STR7 Region. Journal of Molecular Biology *426*, 1753–1765.

915 Bonifacino, J.S., and Glick, B.S. (2004). The Mechanisms of Vesicle Budding and Fusion. Cell *116*, 153–
916 166.

917 Boyadjiev, S.A., Fromme, J.C., Ben, J., Chong, S.S., Nauta, C., Hur, D.J., Zhang, G., Hamamoto, S.,
918 Schekman, R., Ravazzola, M., et al. (2006). Cranio-lenticulo-sutural dysplasia is caused by a SEC23A
919 mutation leading to abnormal endoplasmic-reticulum-to-Golgi trafficking. Nat. Genet. *38*, 1192–1197.

920 Buchan, D.W.A., and Jones, D.T. (2019). The PSIPRED Protein Analysis Workbench: 20 years on. Nucleic
921 Acids Res *47*, W402–W407.

922 Castaño-Díez, D., Kudryashev, M., Arheit, M., and Stahlberg, H. (2012). Dynamo: A flexible, user-friendly
923 development tool for subtomogram averaging of cryo-EM data in high-performance computing
924 environments. Journal of Structural Biology *178*, 139–151.

925 Čopič, A., Latham, C.F., Horlbeck, M.A., D'Arcangelo, J.G., and Miller, E.A. (2012). ER Cargo Properties
926 Specify a Requirement for COPII Coat Rigidity Mediated by Sec13p. Science *335*, 1359–1362.

927 Dokudovskaya, S., Williams, R., Devos, D., Sali, A., Chait, B.T., and Rout, M.P. (2006). Protease
928 Accessibility Laddering: A Proteomic Tool for Probing Protein Structure. Structure *14*, 653–660.

929 Emsley, P., Lohkamp, B., Scott, W.G., and Cowtan, K. (2010). Features and development of Coot. Acta
930 Crystallogr. D Biol. Crystallogr. *66*, 486–501.

931 Fath, S., Mancias, J.D., Bi, X., and Goldberg, J. (2007). Structure and organization of coat proteins in the
932 COPII cage. Cell *129*, 1325–1336.

933 Fromme, J.C., Ravazzola, M., Hamamoto, S., Al-Balwi, M., Eyaid, W., Boyadjiev, S.A., Cosson, P.,
934 Schekman, R., and Orci, L. (2007). The genetic basis of a craniofacial disease provides insight into COPII
935 coat assembly. Dev. Cell *13*, 623–634.

936 Gorur, A., Yuan, L., Kenny, S.J., Baba, S., Xu, K., and Schekman, R. (2017). COPII-coated membranes
937 function as transport carriers of intracellular procollagen I. J. Cell Biol. *216*, 1745–1759.

938 Grant, T., and Grigorieff, N. (2015). Measuring the optimal exposure for single particle cryo-EM using a
939 2.6 Å reconstruction of rotavirus VP6. ELife *4*, e06980.

940 Hagen, W.J.H., Wan, W., and Briggs, J.A.G. (2017). Implementation of a cryo-electron tomography tilt-
941 scheme optimized for high resolution subtomogram averaging. Journal of Structural Biology *197*, 191–
942 198.

943 Hutchings, J., and Zanetti, G. (2019). Coat flexibility in the secretory pathway: a role in transport of bulky
944 cargoes. Current Opinion in Cell Biology *59*, 104–111.

945 Hutchings, J., Stancheva, V., Miller, E.A., and Zanetti, G. (2018). Subtomogram averaging of COPII
946 assemblies reveals how coat organization dictates membrane shape. Nature Communications *9*, 4154.

947 Jin, L., Pahuja, K.B., Wickliffe, K.E., Gorur, A., Baumgärtel, C., Schekman, R., and Rape, M. (2012).
948 Ubiquitin-dependent regulation of COPII coat size and function. Nature *482*, 495–500.

949 Kovtun, O., Leneva, N., Bykov, Y.S., Ariotti, N., Teasdale, R.D., Schaffer, M., Engel, B.D., Owen, D.J.,
950 Briggs, J.A.G., and Collins, B.M. (2018). Structure of the membrane-assembled retromer coat
951 determined by cryo-electron tomography. Nature *561*, 561–564.

952 Kovtun, O., Dickson, V.K., Kelly, B.T., Owen, David.J., and Briggs, J.A.G. (2020). Architecture of the
953 AP2:clathrin coat on the membranes of clathrin-coated vesicles. BioRxiv 2020.01.28.922591.

954 Kremer, J.R., Mastronarde, D.N., and McIntosh, J.R. (1996). Computer visualization of three-
955 dimensional image data using IMOD. Journal of Structural Biology *116*, 71–76.

956 Krissinel, E., and Henrick, K. (2007). Inference of macromolecular assemblies from crystalline state. J.
957 Mol. Biol. *372*, 774–797.

958 Lam, S.D., Das, S., Sillitoe, I., and Orengo, C. (2017). An overview of comparative modelling and
959 resources dedicated to large-scale modelling of genome sequences. Acta Crystallogr D Struct Biol *73*,
960 628–640.

961 Lee, M.C.S., Orci, L., Hamamoto, S., Futai, E., Ravazzola, M., and Schekman, R. (2005). Sar1p N-terminal
962 helix initiates membrane curvature and completes the fission of a COPII vesicle. Cell *122*, 605–617.

963 Liebschner, D., Afonine, P.V., Baker, M.L., Bunkóczi, G., Chen, V.B., Croll, T.I., Hintze, B., Hung, L.-W.,
964 Jain, S., McCoy, A.J., et al. (2019). Macromolecular structure determination using X-rays, neutrons and
965 electrons: recent developments in Phenix. Acta Cryst D *75*, 861–877.

966 Lord, C., Bhandari, D., Menon, S., Ghassemian, M., Nycz, D., Hay, J., Ghosh, P., and Ferro-Novick, S.
967 (2011). Sequential interactions with Sec23 control the direction of vesicle traffic. Nature *473*, 181–186.

968 Ma, W., and Goldberg, J. (2016). TANGO1/cTAGE5 receptor as a polyvalent template for assembly of
969 large COPII coats. PNAS *113*, 10061–10066.

970 Malhotra, V., and Erlmann, P. (2015). The Pathway of Collagen Secretion. Annual Review of Cell and
971 Developmental Biology *31*, 109–124.

972 Mastronarde, D.N. (2005). Automated electron microscope tomography using robust prediction of
973 specimen movements. Journal of Structural Biology *152*, 36–51.

974 Matsuoka, K., Orci, L., Amherdt, M., Bednarek, S.Y., Hamamoto, S., Schekman, R., and Yeung, T. (1998a).
975 COPII-coated vesicle formation reconstituted with purified coat proteins and chemically defined
976 liposomes. Cell *93*, 263–275.

977 Matsuoka, K., Orci, L., Amherdt, M., Bednarek, S.Y., Hamamoto, S., Schekman, R., and Yeung, T. (1998b).
978 COPII-coated vesicle formation reconstituted with purified coat proteins and chemically defined
979 liposomes. Cell *93*, 263–275.

980 Miller, E., Antonny, B., Hamamoto, S., and Schekman, R. (2002). Cargo selection into COPII vesicles is
981 driven by the Sec24p subunit. The EMBO Journal *21*, 6105–6113.

982 Miller, E.A., Beilharz, T.H., Malkus, P.N., Lee, M.C.S., Hamamoto, S., Orci, L., and Schekman, R. (2003).
983 Multiple cargo binding sites on the COPII subunit Sec24p ensure capture of diverse membrane proteins
984 into transport vesicles. Cell *114*, 497–509.

985 Mossessova, E., Bickford, L.C., and Goldberg, J. (2003). SNARE selectivity of the COPII coat. Cell *114*,
986 483–495.

987 Noble, A.J., Zhang, Q., O'Donnell, J., Hariri, H., Bhattacharya, N., Marshall, A.G., and Stagg, S.M. (2013).
988 A pseudoatomic model of the COPII cage obtained from cryo-electron microscopy and mass
989 spectrometry. Nature Structural & Molecular Biology *20*, 167–173.

990 Paraan, M., Bhattacharya, N., Uversky, V.N., and Stagg, S.M. (2018). Flexibility of the Sec13/31 cage is
991 influenced by the Sec31 C-terminal disordered domain. J. Struct. Biol. *204*, 250–260.

992 Pettersen, E.F., Goddard, T.D., Huang, C.C., Couch, G.S., Greenblatt, D.M., Meng, E.C., and Ferrin, T.E.
993 (2004). UCSF Chimera - A visualization system for exploratory research and analysis. Journal of
994 Computational Chemistry *25*, 1605–1612.

995 Qu, K., Glass, B., Doležal, M., Schur, F.K.M., Murciano, B., Rein, A., Rumlová, M., Ruml, T., Kräusslich, H.-
996 G., and Briggs, J.A.G. (2018). Structure and architecture of immature and mature murine leukemia virus
997 capsids. Proceedings of the National Academy of Sciences *115*, E11751–E11760.

998 Saito, K., Chen, M., Bard, F., Chen, S., Zhou, H., Woodley, D., Polischuk, R., Schekman, R., and Malhotra,
999 V. (2009). TANGO1 facilitates cargo loading at endoplasmic reticulum exit sites. Cell *136*, 891–902.

1000 Santos, A.J.M., Nogueira, C., Ortega-Bellido, M., and Malhotra, V. (2016). TANGO1 and Mia2/cTAGE5
1001 (TALI) cooperate to export bulky pre-chylomicrons/VLDLs from the endoplasmic reticulum. J. Cell Biol.
1002 *213*, 343–354.

1003 Sikorski, R.S., and Hieter, P. (1989). A system of shuttle vectors and yeast host strains designed for
1004 efficient manipulation of DNA in Saccharomyces cerevisiae. Genetics *122*, 19–27.

1005 Sillitoe, I., Lewis, T.E., Cuff, A., Das, S., Ashford, P., Dawson, N.L., Furnham, N., Laskowski, R.A., Lee, D.,
1006 Lees, J.G., et al. (2015). CATH: comprehensive structural and functional annotations for genome
1007 sequences. Nucleic Acids Res. *43*, D376-381.

1008 Stagg, S.M., Gürkan, C., Fowler, D.M., LaPointe, P., Foss, T.R., Potter, C.S., Carragher, B., and Balch, W.E.
1009 (2006). Structure of the Sec13/31 COPII coat cage. Nature *439*, 234–238.

1010 Stagg, S.M., LaPointe, P., Razvi, A., Gürkan, C., Potter, C.S., Carragher, B., and Balch, W.E. (2008).
1011 Structural basis for cargo regulation of COPII coat assembly. Cell *134*, 474–484.

1012 Stancheva, V.G., Hutchings, J., Li, X.-H., Santhanam, B., Babu, M.M., Zanetti, G., and Miller, E.A. (2020).
1013 A multivalent fuzzy interface drives reversible COPII coat assembly. BioRxiv 2020.04.15.043356.

1014 Terwilliger, T.C., Ludtke, S.J., Read, R.J., Adams, P.D., and Afonine, P.V. (2020). Improvement of cryo-
1015 EM maps by density modification. BioRxiv 845032.

1016 Townley, A.K., Feng, Y., Schmidt, K., Carter, D.A., Porter, R., Verkade, P., and Stephens, D.J. (2008).
1017 Efficient coupling of Sec23-Sec24 to Sec13-Sec31 drives COPII-dependent collagen secretion and is
1018 essential for normal craniofacial development. J. Cell. Sci. *121*, 3025–3034.

1019 Turoňová, B., Schur, F.K.M., Wan, W., and Briggs, J.A.G. (2017). Efficient 3D-CTF correction for cryo-
1020 electron tomography using NovaCTF improves subtomogram averaging resolution to 3.4 Å. Journal of
1021 Structural Biology *199*, 187–195.

1022 Venditti, R., Scanu, T., Santoro, M., Di Tullio, G., Spaar, A., Gaibisso, R., Beznoussenko, G.V., Mironov,
1023 A.A., Mironov, A., Zelante, L., et al. (2012). Sedlin controls the ER export of procollagen by regulating
1024 the Sar1 cycle. Science *337*, 1668–1672.

1025 Webb, B., and Sali, A. (2017). Protein Structure Modeling with MODELLER. Methods Mol. Biol. *1654*,
1026 39–54.

1027 Wuestehube, L.J., and Schekman, R.W. (1992). Reconstitution of transport from endoplasmic reticulum
1028 to Golgi complex using endoplasmic reticulum-enriched membrane fraction from yeast. Meth.
1029 Enzymol. *219*, 124–136.

1030 Zanetti, G., Pahuja, K.B., Studer, S., Shim, S., and Schekman, R. (2012). COPII and the regulation of
1031 protein sorting in mammals. Nature Cell Biology *14*, 20–28.

1032 Zanetti, G., Prinz, S., Daum, S., Meister, A., Schekman, R., Bacia, K., and Briggs, J.A.G. (2013). The
1033 structure of the COPII transport-vesicle coat assembled on membranes. Elife *2*, e00951.

1034 Zheng, S.Q., Palovcak, E., Armache, J.-P., Verba, K.A., Cheng, Y., and Agard, D.A. (2017). MotionCor2:
1035 anisotropic correction of beam-induced motion for improved cryo-electron microscopy. Nature
1036 Methods *14*, 331–332.

1037 Zimmermann, L., Stephens, A., Nam, S.-Z., Rau, D., Kübler, J., Lozajic, M., Gabler, F., Söding, J., Lupas,
1038 A.N., and Alva, V. (2018). A Completely Reimplemented MPI Bioinformatics Toolkit with a New HHpred
1039 Server at its Core. Journal of Molecular Biology *430*, 2237–2243.

1040

Figure1

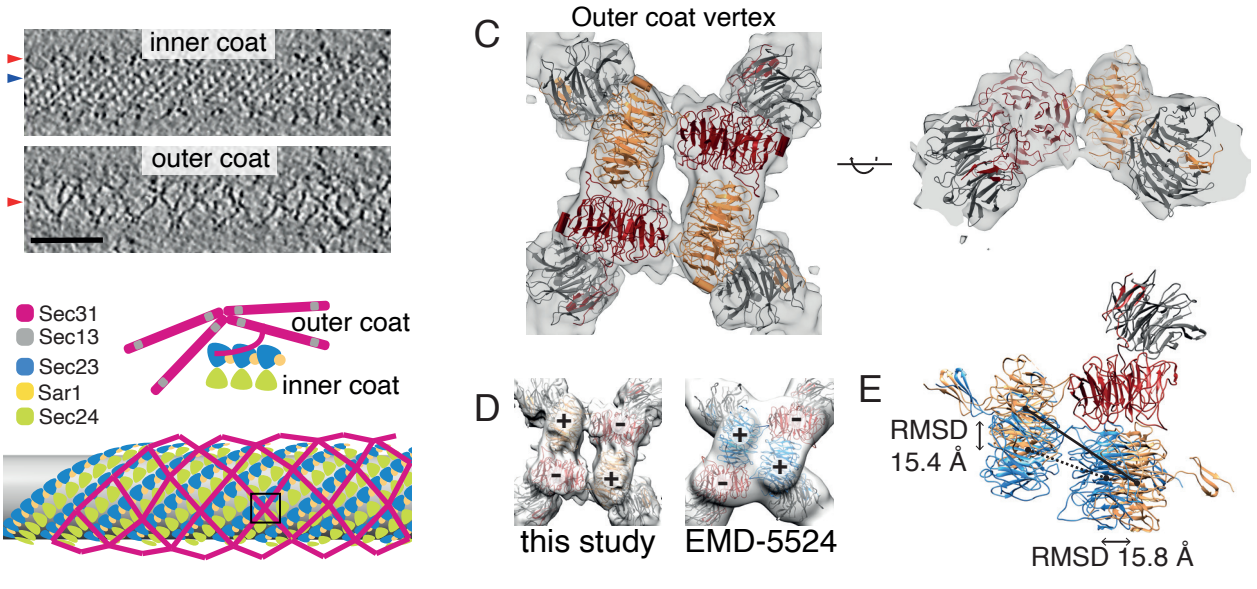
A
inner coat
outer coat
B
Sec31
Sec13
Sec23
Sar1
Sec24
outer coat
inner coat
C
Outer coat vertex
D
+
-
this study
EMD-5524
E
RMSD
15.4 Å
RMSD 15.8 Å

Figure2

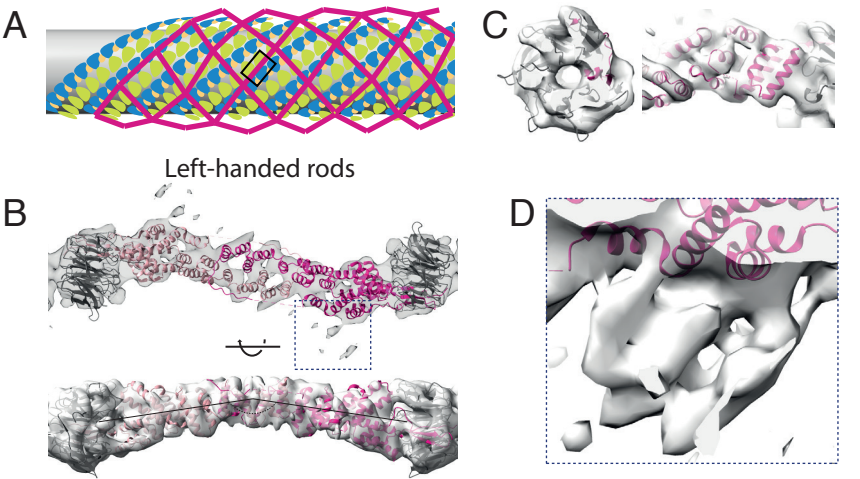

Figure3

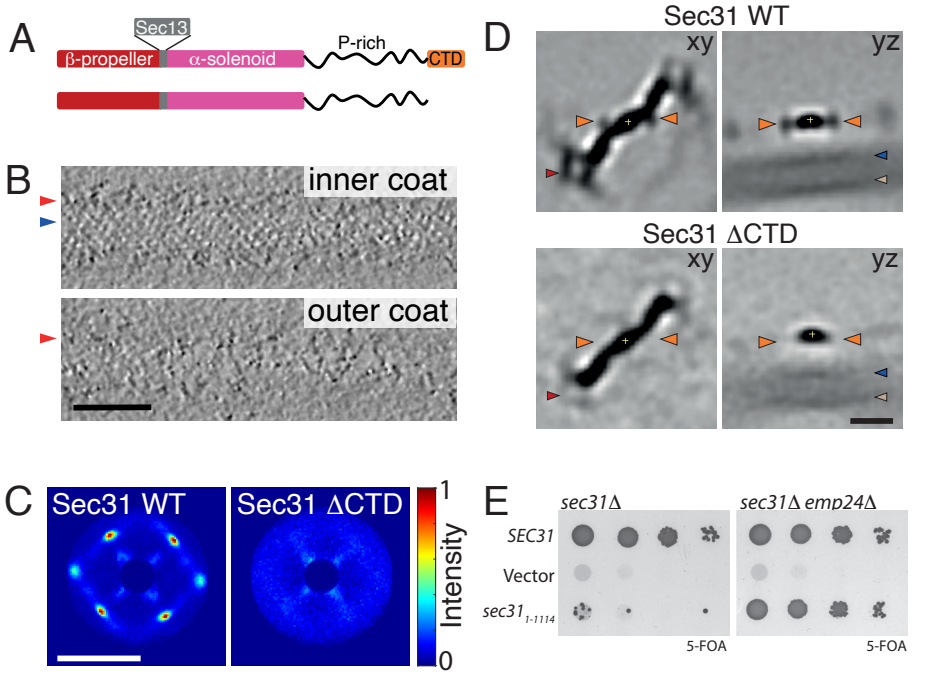
A
Sec13
β-propeller
α-solenoid
P-rich
CTD
B
inner coat
outer coat
C
Sec31 WT
Sec31 ΔCTD
1
Intensity
0
D
Sec31 WT
xy
yz
Sec31 ΔCTD
xy
yz
E
sec31Δ
sec31Δ emp24Δ
SEC31
Vector
sec31 1-1114
5-FOA
5-FOA

Figure4

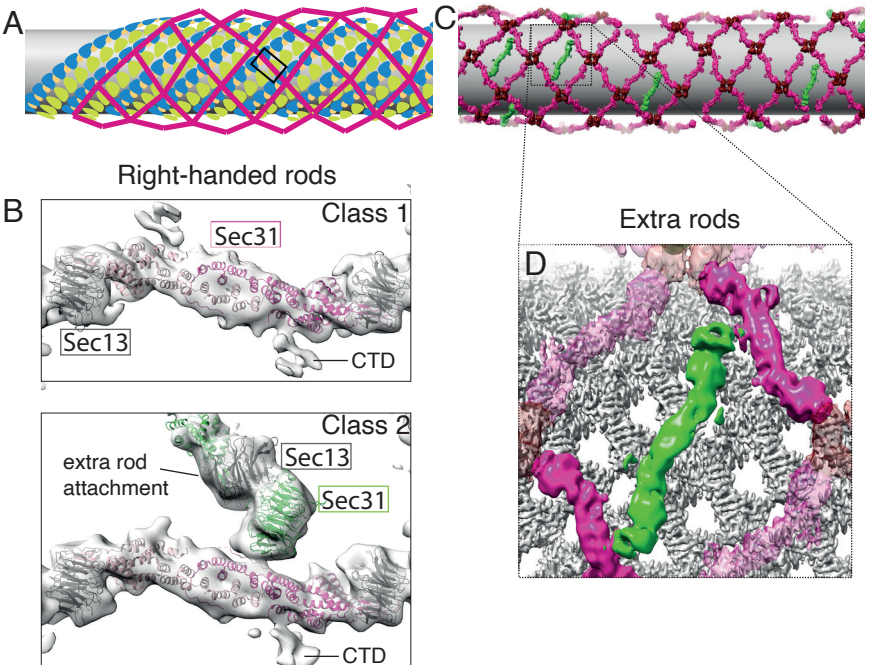
A
C
Right-handed rods
B
Class 1
Sec31
Sec13
CTD
Class 2
extra rod
attachment
Sec13
Sec31
CTD
Extra rods
D

Figure5

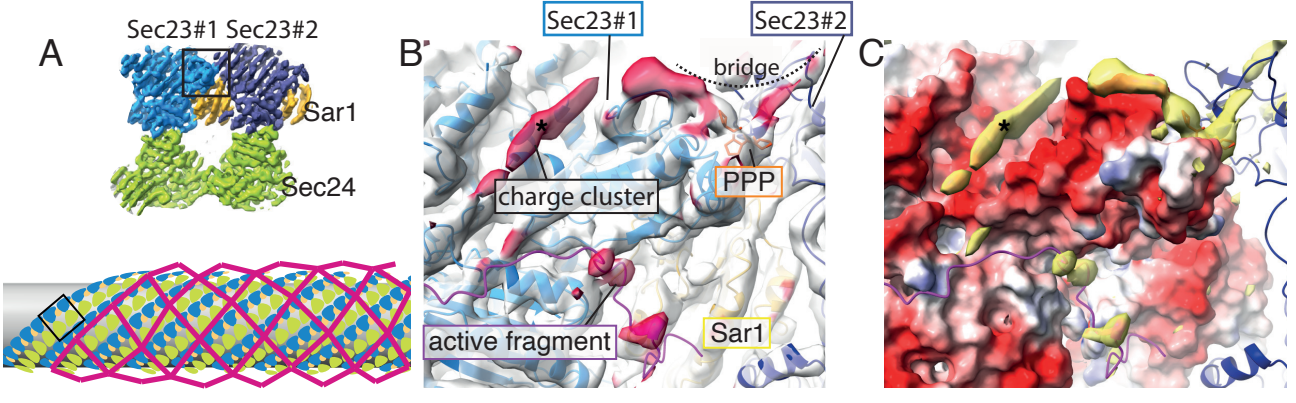
A
Sec23#1 Sec23#2
Sar1
Sec24
B
Sec23#1
Sec23#2
bridge
charge cluster
PPP
active fragment
Sar1
C

Figure6

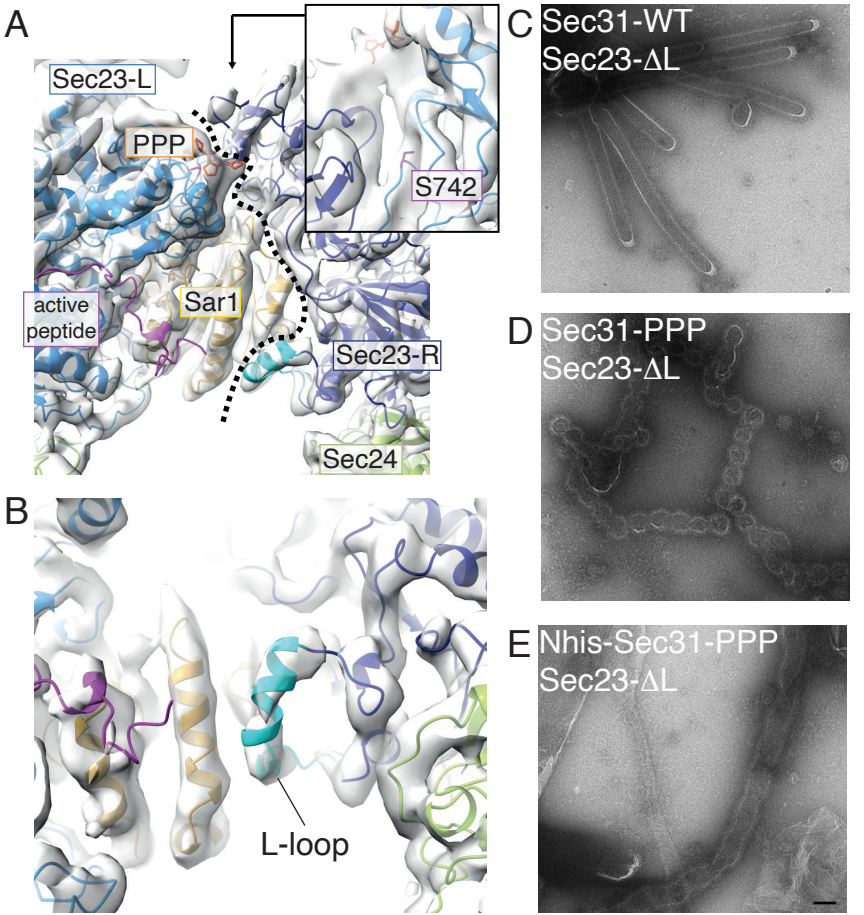
A
Sec23-L
PPP
S742
active peptide
Sar1
Sec23-R
Sec24
B
L-loop
C
Sec31-WT
Sec23-ΔL
D
Sec31-PPP
Sec23-ΔL
E
Nhis-Sec31-PPP
Sec23-ΔL

Figure7

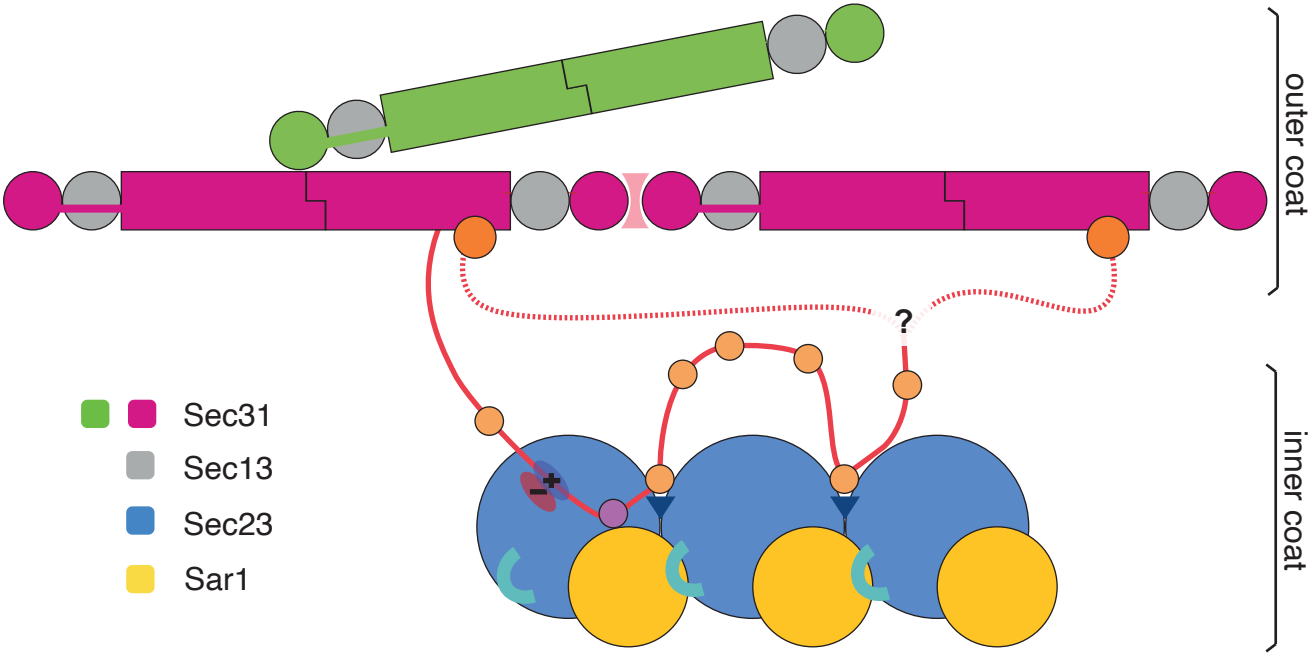

Mapped interactions

outer coat:	inner-outer coat:	inner coat:
Sec31 vertex	PPP	PPP
Sec31 CTD	Catalytic fragment	Sec23-Sec23
Sec31 extra rod	Charged patch	Sar1-Sec23 (L-loop)

Supplementary Figure 1

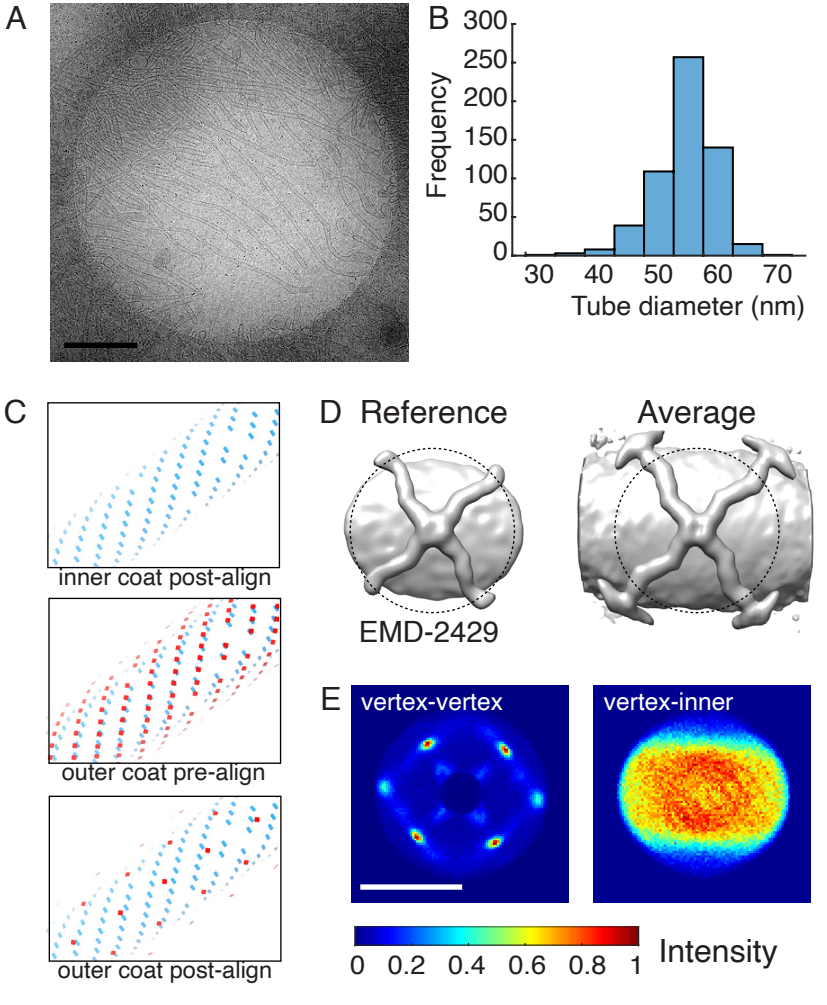

Supplementary Figure 2

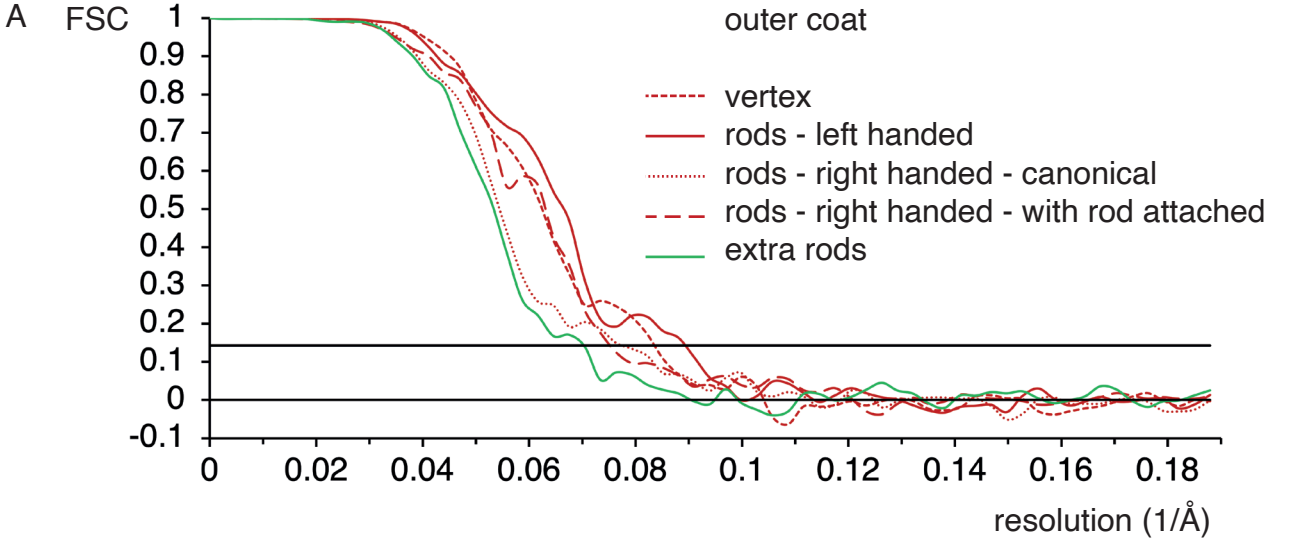

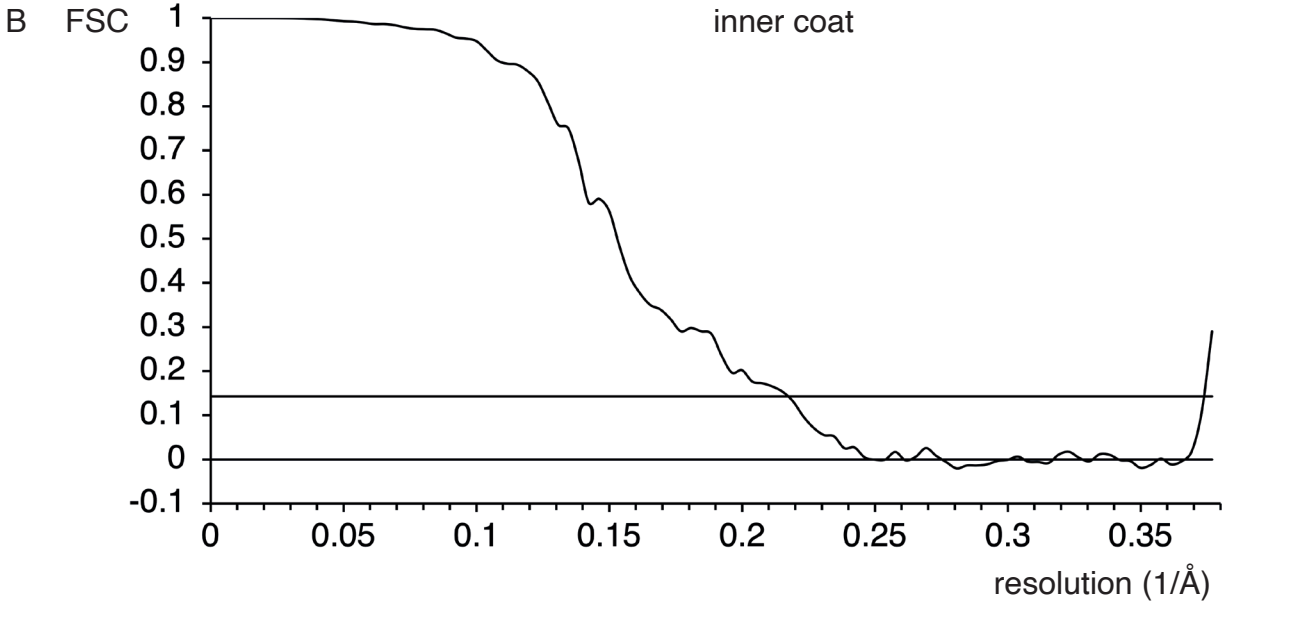

Supplementary Figure3

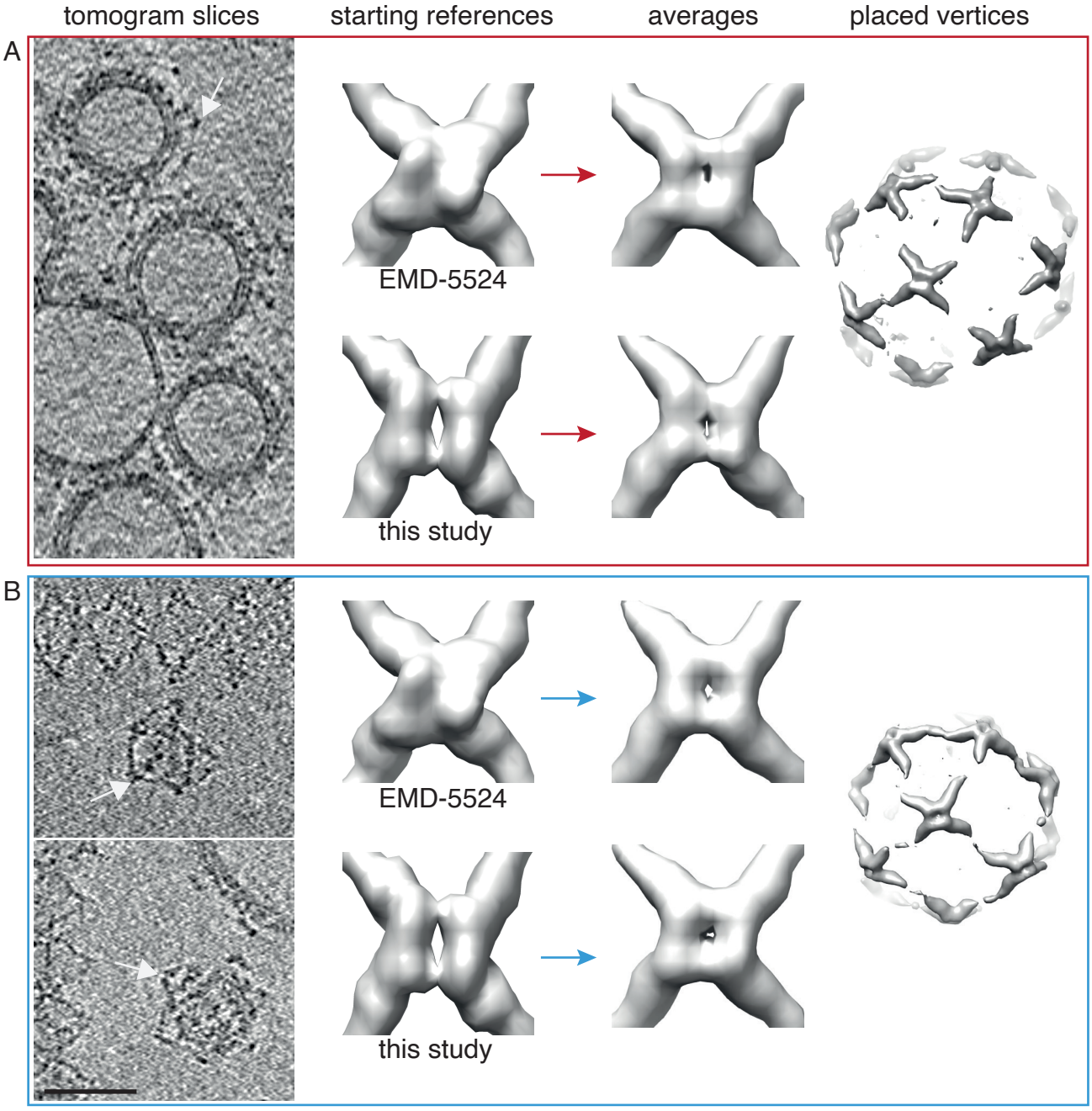

Supplementary Figure 4

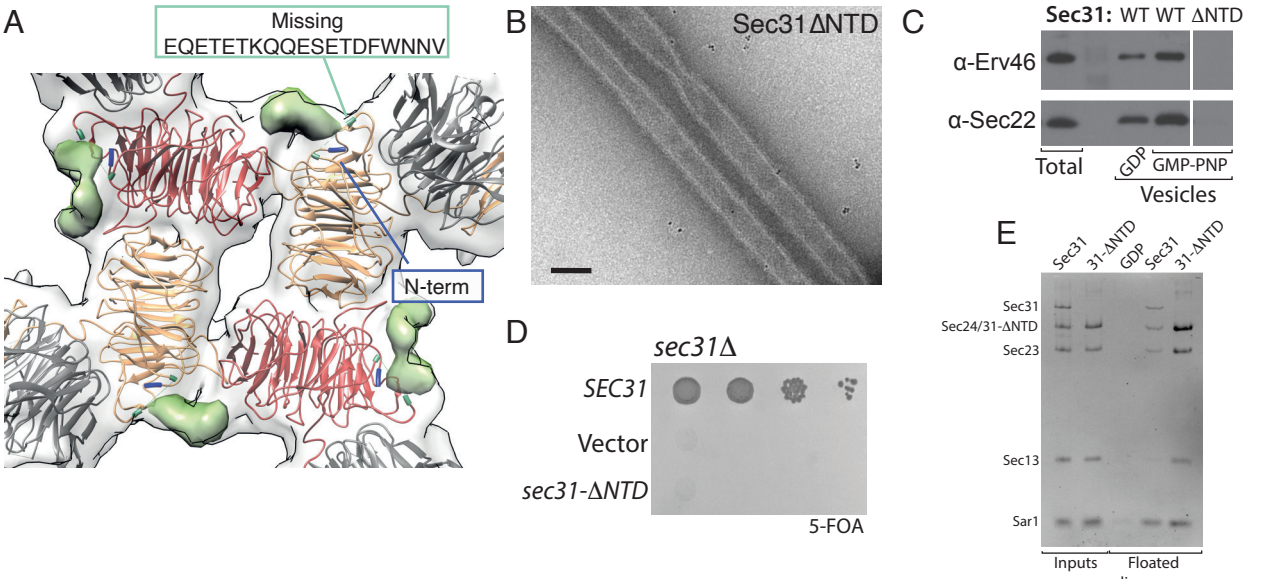

Supplementary Figure 5

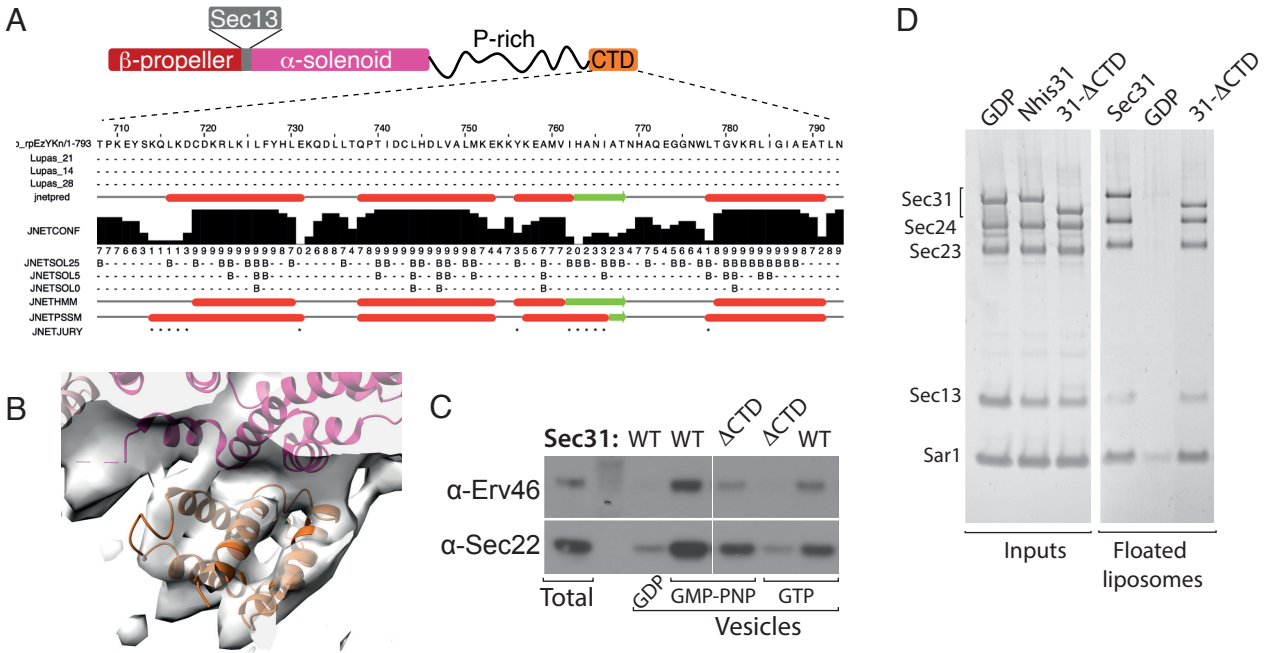

Supplementary Figure 6

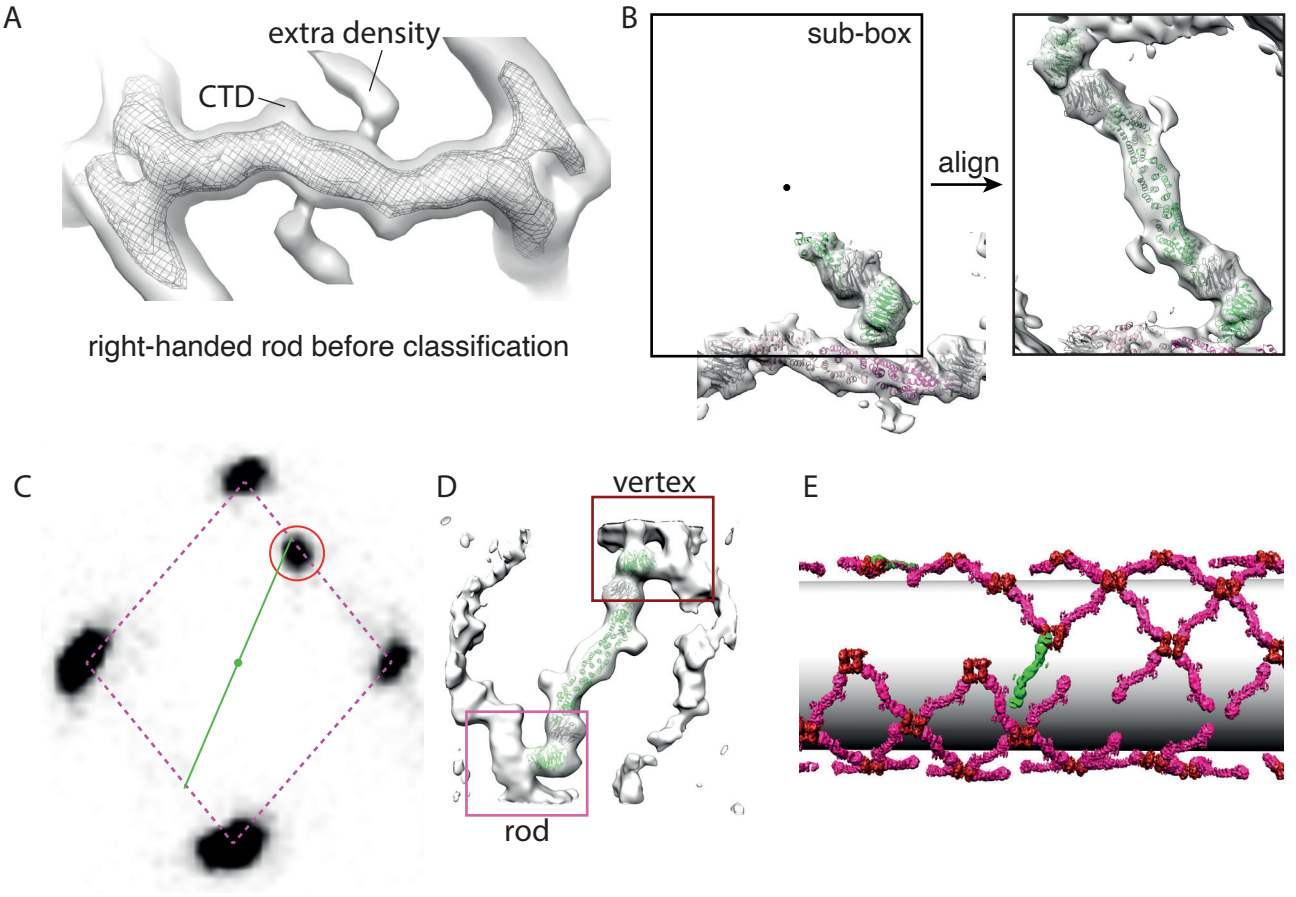
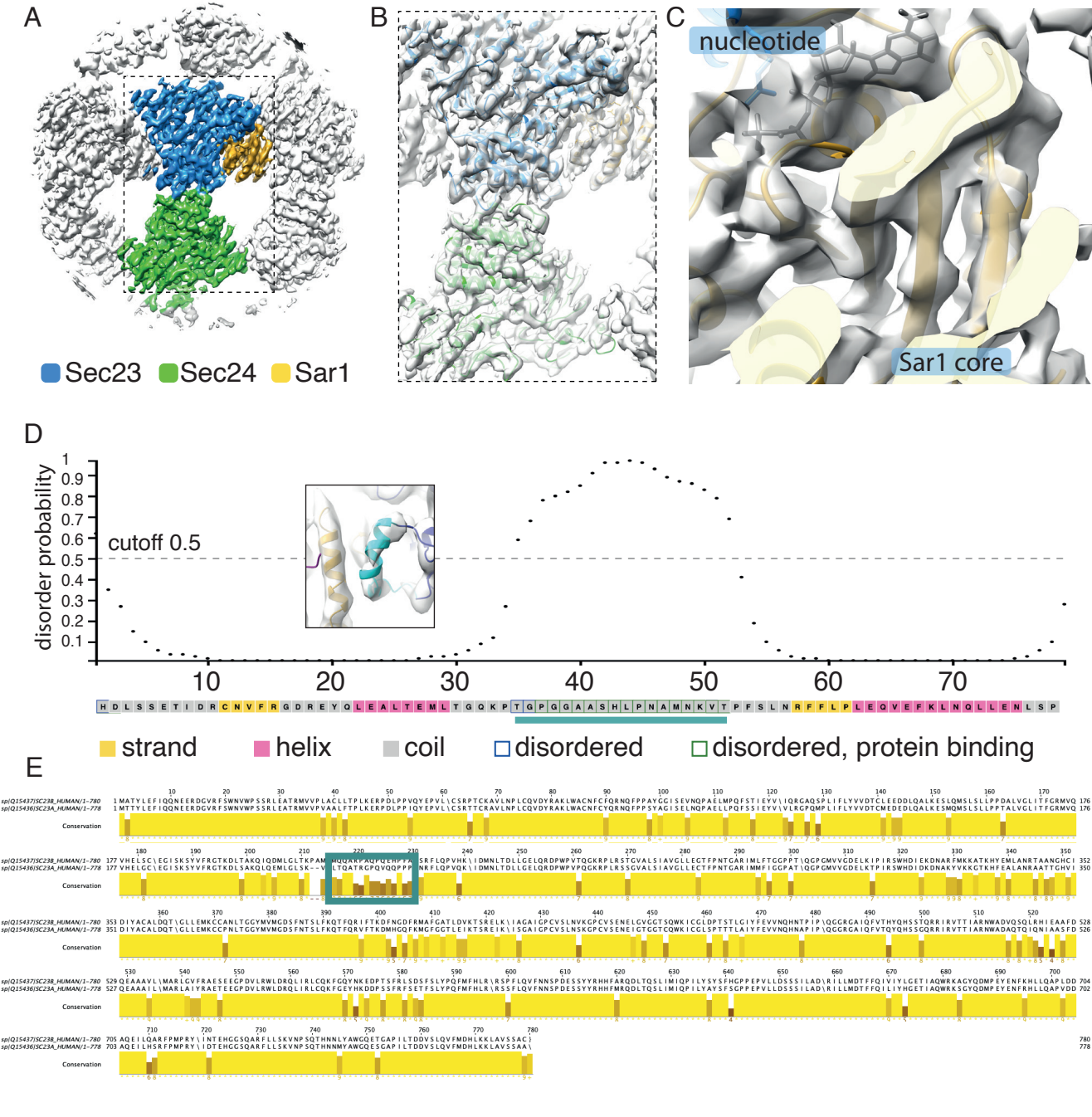
Supplementary Figure 7